Effect of Substrate on In-flight Particle Characteristics in Suspension Plasma Spraying

KOUROSH POURANG

A Thesis

in

the Department

of Mechanical and Industrial Engineering

Presented in Partial Fulfillment of the Requirements
for the Degree of Master of Applied Science (Mechanical Engineering) at
Concordia University
Montreal, Quebec, Canada

Summer 2015

Concordia University

CONCORDIA UNIVERSITY
School of Graduate Studies

This is to certify that the thesis prepared

By: Kourosh Pourang

Entitled: Effect of Substrate on In-flight Particle Characteristics in Suspension Plasma Spraying

and submitted in partial fulfillment of the requirements for the degree of

Master of Applied Science (Mechanical Engineering)

complies with the regulations of the University and meets the accepted standards with respect to originality and quality.

Signed by the final examining committee:

R. Bhat Chair

M. Paraschivoiu Examiner

F. Haghighat Examiner

A. Dolatabadi and C. Moreau Supervisor

Approved by _____
Chair of Department or Graduate Program Director

_____
Dean of Faculty

Date _____

Abstract

Thermal spray technology is a widely used technique in industry in which surfaces of materials are coated by spraying a wide range of metals or ceramics. Considering the growing interest in building nanostructured coatings due to their significant characteristics a new technique called suspension plasma spraying is developed. In this method, a coating is formed by injecting a suspension of nano or sub-micron sized particles into a plasma flame. Obtaining a uniform coating on mechanical parts is one of the industrial challenges in suspension plasma spraying. Through a three dimensional numerical analysis, this study is aimed at providing a better understanding of the effect of substrate position and curvature on in-flight particle temperature, velocity and trajectory. The high temperature and high velocity plasma flow is simulated inside the plasma torch using a uniform volumetric heat source in the energy equation. The suspension of yttria stabilized zirconia (YSZ) particles is used here due to its vast applications in forming thermal barrier coatings. Suspension is molded in this study as a multicomponent droplet while catastrophic breakup regime is considered for simulating the secondary break-up when the suspension interacts with the plasma flow. A two-way coupled Eulerian-Lagrangian approach along with a stochastic discrete model was used to track the particle trajectory. Particle size distribution in the vicinity of the substrate at different standoff distances has been investigated. Then the effect of substrate curvature on in-flight particle characteristics is discussed. The results show that sub-micron particles obtain higher velocity and temperature compared to the larger particles. However, due to the small Stokes number associated with sub-micron particles, they are more sensitive to the change of the gas flow streamlines in the vicinity of the substrate.

ACKNOWLEDGEMENTS

Hereby I would like to express my sincere gratitude and appreciation to Professor Ali Dolatabadi and Professor Christian Moreau for without their continuous help and support this research would not have been possible. Their dedication and patience has led me through this journey from the very beginning to the end and their guidance has always shed light to the challenges and hardships of this study.

Special thanks to Mohammad Reza Attarzadeh, Mahdi Jadidi and Milad Mousavi for their help and support whenever problems and impediments were encountered.

Last but not least, to my family for without their love, help and support, my master studies would not have been possible; thank you for your continuous encouragements to pursue my dreams and always believing in me.

Contents

List of Figures

Chapter 1

Chapter 2

Chapter 3

List of Tables

Chapter 2

Chapter 3

LIST OF SYMBOLS

A	Cross sectional area of the particles	[m^2]
c	Specific heat	[J/kg.K]
C	Concentration of the dispersed phase	
C_D	Drag coefficient	
D	Particle diameter	[m]
DE	Deposition efficiency	
e	Internal energy	[J]
f	Force acting on dispersed phase per unit volume	[N/m^3]
F_b	Body force per unit mass of particles	[N/kg]
F_D	Drag force	[N]
g	Gravitational acceleration	[m/s^2]
h	Specific enthalpy	[J/kg]
h_p	Particles convective heat transfer coefficient	[$W/m^2.K$]
I	Unit tensor	
k	Thermal conductivity	[W/m.K]
K	Momentum exchange coefficient	
L	Flow characteristic length	[m]

$\boldsymbol{M, m}$	Mass	[kg]
$\boldsymbol{Ma}$	Mach number	
$\boldsymbol{n}$	Number density of the dispersed phase	[m^{-3}]
$\boldsymbol{Nu}$	Nusselt number	
$\boldsymbol{p}$	Pressure	[Pa]
$\boldsymbol{Pr}$	Prandtl number	
$\boldsymbol{q}$	Heat flux	[W/m^2]
$\boldsymbol{R}$	Energy exchange coefficient	
$\boldsymbol{R_g}$	Universal gas constant	[J/kg.K]
$\boldsymbol{Re}$	Reynolds number	
$\boldsymbol{St}$	Stokes number	
$\boldsymbol{t}$	Time	[s]
$\boldsymbol{T}$	Temperature	[K]
$\boldsymbol{U, u}$	Velocity vector	[m/s]
$\boldsymbol{V}$	Volume	[m^3]
$\boldsymbol{z}$	Local loading	
$\boldsymbol{Z}$	Overall loading	

Greek Symbols

$\boldsymbol{\alpha}$	Phase indicator function

γ	Specific heat ratio	
ε	Rate of strain tensor	
θ	Volume fraction	
μ	Dynamic viscosity	[kg/m.s]
ρ	Density	[kg/m^3]
τ	Deviatoric stress tensor	
τ_V	Momentum response time	[s]
τ_T	Thermal response time	[s]
υ	Kinematic viscosity	[m^2/s]

1. Introduction

In This chapter

In this chapter, a brief introduction to thermal spray technology will be given. Furthermore, suspension plasma spraying technique will be discussed in detail. Moreover, objectives and significance of this work will be presented.

The application of coatings on the surface of various components in industry has been pursued for many years. The purpose of applying coatings is to improve the surface properties of substrates or even add new ones without changing the core property of the main part. Providing higher temperature exposure as done in thermal barrier coatings, a higher fatigue life, reducing wear due to corrosion or even creating hydrophobic surfaces by introducing surface roughness are few examples of improving the functionality of parts and components used in various industries.

Although there are various techniques for applying coatings on surfaces, the focus here is on the thermal spray technology. Thermal spraying is defined as group of processes in which fine metallic or non-metallic materials in molten or semi molten condition are deposited on surfaces to create coatings [1]. This method is used widely in industry since almost any material that can be melted, can be applied to the surface of the part of the interest with no significant amount of power required. Based on how the required energy for melting the coating material is provided, thermal spray is divided into different categories. This energy can be provided by electrical discharge, combustion or even high pressure gases [1].

Among thermal spray processes, plasma spraying processes are commonly used in industry. A plasma gun consists of a copper anode and a tungsten cathode. In this technique, high electrical energy is produced inside a plasma gun due to electrical discharge between the anode and cathode. This energy leads to ionization of an incoming gas flow inside the gun which leads to the formation of a plasma (Figure1.1^{1}). The temperature of the plasma

gas inside the plasma gun can reach high values such as 20,000 K while the exhausting[1] plasma gas from the nozzle exit usually has a temperature between 8000 to 14000 K and

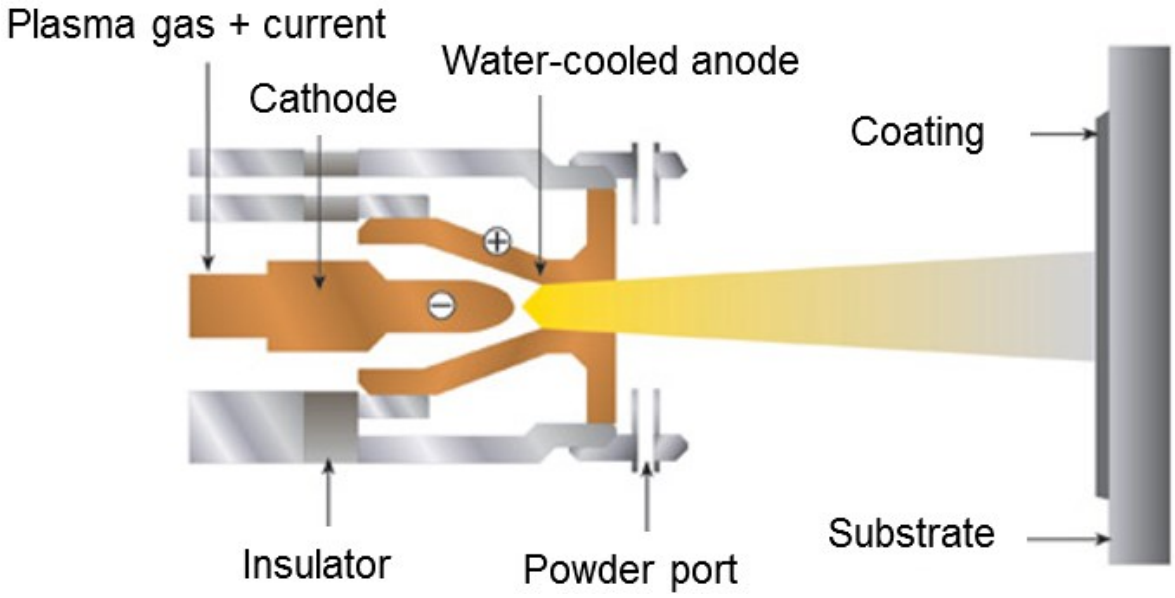

Figure1.1 Schematic of an atmospheric plasma spray process

velocities range from 500 to 2800 m/s depending on plasma gun operation conditions [2]. The plasma gas may comprise a single (e.g. Ar) or a mixture of different gasses (Ar-H_2, Ar-He, Ar-He-H_2, etc.). In atmospheric plasma spraying (APS), the plasma exhausts to open air environment. Since the feedstock is in the form of powder, an auxiliary carrier gas is needed to transport the feedstock into the flame so that the particles are accelerated and heated before impacting on the substrate. These coating particles usually have a size distribution in the range of 10 to 110 μm and, depending on the process, they can be injected in radial or axial direction with respect to the plasma gas flow [2].It has been

[1] Extracted from http://www.amphardchrome.co.uk/plasma-spraying

shown that during long-term experiment, particle state along with the plasma gun condition and spray time are important parameters in controlling the coating characteristics [3].

1.1. Suspension plasma spraying (SPS)

In the past decade, producing nano-structure coatings has been the focus of many research topics due to their notable properties such as improved dimensional stability or lower thermal diffusivity compared to the conventional ones [2]. One of the challenges in this area is finding a way to inject these nano-sized particles into the gas flow. To address this problem a relatively new technique called suspension plasma spraying is being used. In this technique, suspension of nano- or submicron sized particles in a base fluid (usually ethanol or water) is injected into the plasma plume in a form of liquid jet or train of fragmented droplets [4]. Both axial and radial injections of the liquid feedstock are used to transport the suspension into the plasma flow. The use of a liquid carrier is to provide the required momentum for the small sized particles to penetrate inside the plasma. However, transport of suspension into plasma flow is a complex phenomenon. These phenomena, as can be seen in Figure 1.2, include penetration and atomization of the suspension, vaporization of the solvent, acceleration and heating of the submicron particles, particle agglomeration, particles evaporation and finally particle impact, spreading and solidification. There are various parameters that affect the properties of the SPS coatings such as torch operating condition, plasma arc fluctuation, suspension jet/droplets penetration, fragmentation, and evaporation [5]. The suspension drops penetrate inside the plume if their momentum density ($\rho_l v_l^2$) is higher than that of the gas flow ($\rho_g v_g^2$) .The

fragmentation of the suspension starts when instabilities induced by the aerodynamic forces overcome the surface tension force of the liquid suspension. Breakup of the liquid feedstock is characterized by the Weber number ($\frac{\rho v^2 l}{\sigma}$) which is the ratio of the inertia force to the

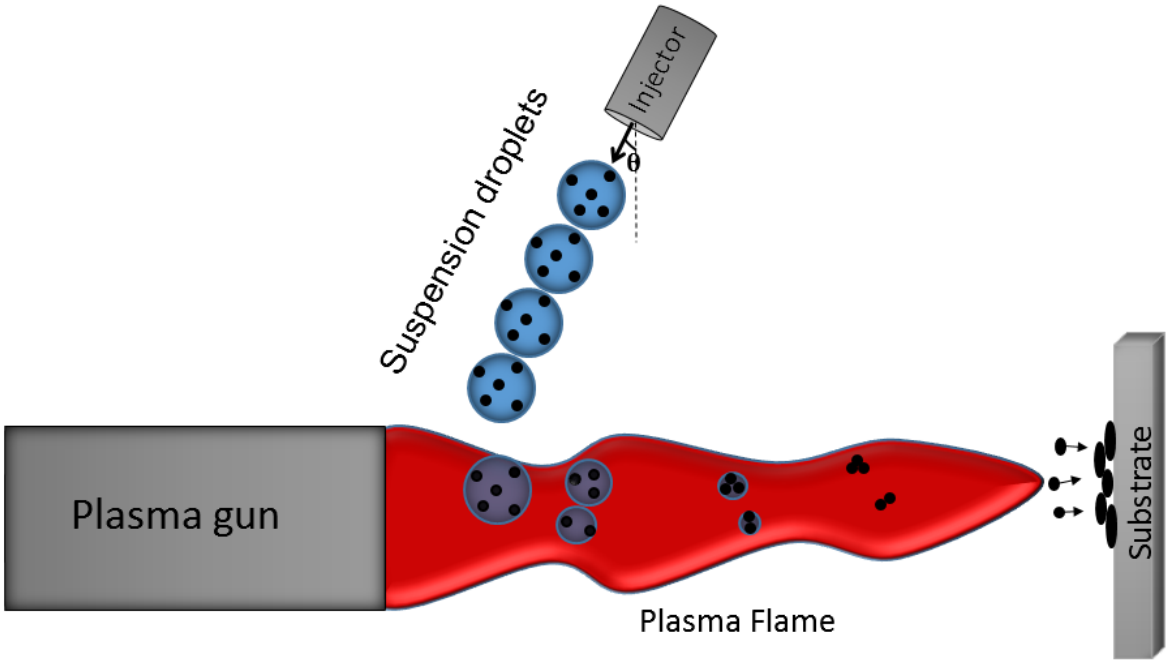

Figure 1.2 Phenomena involved in radial suspension injection

surface tension force. Moreover in the radial injection case, droplet jet velocity and orientation of the injector (angle) are found to be important parameters that affect the heat and momentum transfer [6]. Furthermore, it was observed that particles' velocity and temperature are mostly affected by the actual plasma torch conditions and feed stock parameters such as powder size distribution or particle concentration, respectively [7].

1.2. Previous works

Recently, on-line particle diagnostics in plasma spraying process has been one of the interesting subjects due to the direct correlation between the particle conditions (velocity, temperature and size) upon impact on the substrate and the resulting coating characteristics. In spite of several available experimental diagnostic systems (DPV-2000, Accuraspray-g3, etc.), their applications are limited by some factors such as size of the sprayed particles and the spray distance [8]. The intensity of the plasma radiation, speed of the occurrence of the droplets fragmentation along the high temperature and velocity gradients within plasma are among phenomena that make these experimental measurements extremely difficult [5].

Alongside the experimental works, numerical study of plasma spray processes has been proven to be a useful tool to find a path to a better understanding of these complex phenomena that are involved in this deposition processes and overcome the above challenges.

In early simulation works, the plasma flow was modeled using constant or parabolic profiles as inlet boundary conditions for the plasma temperature and velocity at the torch exit [9-15]. In [9], the authors simulate the turbulent argon plasma jet flowing in to the cold air by utilizing classical k-ε model and the same profiles mentioned above. Afterwards, two main approaches were followed in the literature to model the plasma flow within the plasma torch. The first group relied on using the Joule's heating effect concept for modelling the steady or, in more complex manner the transient plasma flow [16-21]. The second group used a more global approach to capture the arc movement and the consequent transient plasma flow by solving the equations of fluid mechanics coupled with

electromagnetic ones [22]. In most of these simulations local thermal equilibrium assumption, in which all the species inside the plasma gas are considered at the same temperature, was considered.

Due to the large gas acceleration and shear velocity and temperature gradient inside the torch accompanied by electromagnetic forces, flow inside the torch is turbulent and unstable. Thus, choosing a turbulence model that can best describe the plasma flow dynamic is of great importance. The most accurate approach for modelling turbulent flows is known as direct numerical simulation approach or DNS in which all the scales of the flow is resolved without any approximation. The large computational cost (computing power) of DNS has brought the attention to the other approaches such as large eddy simulation (LES) or Reynolds-averaged Navier-Stokes (RANS) models. When the movement of the arc inside the torch is considered in the simulation, LES provides more accurate results. However, for the cases in which plasma gas is assumed to be steady, RANS models provide sufficient accuracy [21]. RANS models are used for turbulence modelling in the literature by far most compared to other approaches. Within the various RANS models, a two equation k-ε model has been widely used due its computational simplicity compared to other more complex models.

Remesh et al. [16] simulated the plasma heating by adding a constant energy source in the energy equation. The classical k-ε turbulence model alongside the plasma gun efficiency of 63% were used in this study. All the studies that used the classical k-ε turbulence model to simulate plasma flow showed an underestimation in predicting the plasma high temperature core. To address this problem, Bolot et al. [10] proposed that a sink term should be added in k equation since the classical k-ε built in model in FLUENT software

underestimates the high plasma temperature plasma core. In another study [11], the authors showed simulations based on Reynolds stress turbulence model produces similar results to the modified k-ε model in [9].

Due to the transient nature of the plasma flow, Meillot et al. [17] proposed a time dependent moving energy volume to take into account the plasma arc movement within the torch.

Most of the aforementioned studies also considered the effect of injection of particles inside the plasma flow by using a Lagrangian approach. In this approach, a large number of the injected particles that can change momentum, mass and energy within the flow in which they are tracked. In [14], authors used the same approach to study the change in velocity, temperature and diameter of multi-sized particles injected in a plasma plume. Throughout the literature, it has been shown that fragmentation of liquid feed-stock is one of the major parameters that has a great impact on coating characteristics. Shan et al. [12] simulated the plasma flow alongside droplet collision and break up by utilizing Re-Normalization Group (RNG) k-ε, with Taylor Analogy Breakup (TAB) model. They reported that both droplet collision and break up should be considered in the simulation. By injecting different size water droplets into the transient plasma, Marchand et al. [18] investigated the evolution of droplets' Weber number along with their trajectories. The work [18] showed a need for a break up model which can adapt itself to the changes of the Weber number as the droplet penetrates into the plasma plume. Jabbari et al. [14] developed a model to investigate the suspension atomization, evaporation and break up within an argon plasma flow. In this study, plasma flow exiting the torch was modeled by assuming a parabolic velocity and constant temperature profiles.

Due to dominant effect of primary atomization of suspension jet in SPS process, there has been an increasing interest in simulating liquid atomization in plasma spraying by using more accurate approaches such as volume of fluid (VOF) technique. The advantage of this technique is that it can solve the fragmentation of liquid in small scales rather than using empirical correlations. However the drawback of this approach is its high computational cost and computer power. An example of this approach is the work of Meillot et al. [19] in which fragmentation of the injected liquid feedstock in a steady plasma was simulated in a in small zone 4mm×2.56mm×1mm in front of the nozzle exit .

It is a known fact that the presence of a substrate would affect the fluid flow and particles' trajectories that are injected into the plasma flow especially in the vicinity of the substrate. Thus, the effect of inclusion of a substrate on the plasma flow and the particles' trajectories has been investigated both experimentally and numerically. Kang et al. [20] studied the effect of adding a flat substrate on the behavior of injected in-flight particles near the substrate. They showed that the zone influenced by the substrate is rather small and particle parameters are mainly unaffected and similar to those of the free jet case for particle sizes ranging from 22 to 125 μm. In another study with the same conditions [21], the authors investigated the effect of inclusion of a curved substrate; they suggested that there is a threshold for particle diameter (10 μm) above which particles are unsusceptible to the flow. Selvan et al. [13] investigated the thermal exchange between the Ar-N_2 plasm jet and substrate since substrate heating affects the microstructure of coating in plasma spray process. By using a 3D model alongside the shear stress transport (SST) k-ω turbulence model and parabolic profiles, authors concluded that there is a direct relationship between the heat flux to the substrate and the plasma gas flow rate [13].

Recently the effect of adding a flat substrate on an argon plasma flow with the same conditions and assumptions used in [14] was investigated in SPS process by Jadidi et al. [15]. They analyzed the effect of standoff distance on the impact condition of submicron particles and concluded that due to the stagnation region formed near a flat plate many small size particles would get diverted especially for shorter standoff distances.

1.3. Objectives

The main motivation for the current study is to address the technological challenges to obtain a repeatable and controllable SPS coatings on various substrate shapes. The objectives of this work are summarized below

1. Simulating suspension injection and its interaction with the plasma flow including penetration, atomization, evaporation and solid particles formation.
2. Investigating the effect of insertion of substrate on the plasma flow and particles characteristics especially upon impact.
3. Investigating the effect of changing the substrate standoff distance and changing the substrate curvature on particles characteristics upon impact.
4. Investigating the effect of changing the suspension feed rate on in-flight particle characteristics.

2. Methodology

In this chapter

In this chapter, an overview of the governing equations for both continuous and disperse phases are presented. Furthermore, assumptions and boundary conditions related to this work are discussed.

This study consists of two main parts. In the first part (Eulerian), the solution to the continuous gas phase is obtained by solving the governing equations. Then, the dispersed phase is introduced and solved by using the calculated flow field in the first part.

2.1. Continuous phase

For the continuous phase the Local thermal equilibrium (LTE) assumption is considered everywhere inside the computational domain. By the LTE assumption, the kinetic energy of the species within the plasma gas is categorized by a single temperature. The plasma is considered as a continuous Newtonian compressible chemically inert gas with temperature dependent thermodynamic and transport properties. These properties where extracted from [24] and fitted in to the piecewise profiles.

2.1.1. Governing equations

Mass conservation equation

The continuity or mass conservation equation can be written as follows

$$\frac{\partial \rho}{\partial t} + \nabla . \left(\rho \vec{v} \right) - \omega_m \tag{2-1}$$

This is a general form of mass conservation equation valid for both incompressible and compressible flows. The source term S_m is the added mass to the continuous phase.

Momentum conservation equation

The general form of momentum conservation equation is as follows

$$\frac{\partial}{\partial t}\left(\rho\vec{v}\right)+\nabla\cdot\left(\rho\vec{v}\vec{v}\right)=-\nabla p+\nabla\cdot\left(\bar{\bar{\tau}}_{eff}\right)+\rho\vec{g} \tag{2-2}$$

where in 2-2, p is the static pressure, $\bar{\bar{\tau}}$ is the stress tensor as shown below and $\rho\vec{g}$ is the gravity force

$\bar{\bar{\tau}}$ is obtained from;

$$\bar{\bar{\tau}}_{eff}=\mu_{eff}\left[\left(\nabla\vec{v}+\nabla\vec{v}^{T}\right)-\frac{2}{3}\nabla\cdot\vec{v}I\right] \tag{2-3}$$

In equation 2-3, μ_{eff} is the effective viscosity which is the summation of molecular viscosity (μ) and turbulent eddy viscosity (μ_t), I is the unit tensor and the second term on the right-hand side is for effect of the volume dilation which accounts for the changes in the volume [25].

Energy equation

The energy equation is as follow:

$$\frac{\partial}{\partial t}(\rho E)+\nabla .\left(\vec{v}(\rho E+p)\right)=\nabla\left(k_{eff}\nabla T+\tau_{eef}.\vec{v}\right)+S_E \tag{2-4}$$

k_{eff} represents the effective conductivity and S_E ,is the energy source term. The first part of the right-hand side in 2-4, accounts for the energy transfer due to conduction and the second part represents the heat transfer due to the viscous dissipation. Furthermore, in equation 2-4, *E,* is defined as follows [25].

$$E = h - \frac{P}{\rho} + \frac{V^2}{2} \tag{2-5}$$

Equation of State

To close the above system of equations and take into account the effect of compressibility, the equation of state for ideal gas is used and shown as below

$$p = \rho R_g T \tag{2-6}$$

Species transport equation

After solving the conservation equation for a chemical species, to solve the convection-diffusion equation for each species a local mass fraction for each species should be predicted, Y_i. This equation takes the following general form.

$$\frac{\partial}{\partial t}(\rho Y_i)+\nabla .\left(\rho \vec{v} Y_i\right)=-\nabla .\vec{J}_i+R_i+S_i \tag{2-7}$$

In 2-7, R_i is the rate of production of species *i*, by chemical reaction, which is zero in our case since there is no reaction. S_i, is the source term representing the rate of creation by adding from the dispersed phase. This equation should be solved for N-1 species where N is the number of total species [25].

2.1.2. Turbulence modeling

Due to the electrical discharge occurring inside a plasma gun, a great amount of energy transfers to the incoming gas flow. Transferring this great amount of energy to the gas will lead to high gradient gas temperature, sudden expansion and rapid acceleration of the gas and eventually generating a turbulent gas flow. Turbulence is further affected by inclusion of the cold substrate in the domain. Further downstream of the plasma gun, flow diversion, rotation and high velocity gradients in the vicinity of the substrate will create a high turbulent area. Thus, choosing a turbulence model that is able to predict the length of the plasma potential core correctly alongside capturing the flow changes near the substrate is of great importance here.

Due to the large computational cost associated with DNS and LES, RANS models have been used frequently in simulating plasma spraying [23]. Throughout the various models within RANS, RNG *k*-*ε* and Reynolds stress models have shown a better prediction for the plasma high temperature core compared to the rest. Reynolds stress model is chosen for

this study since compared to the *k-ε* family, it has a greater potential for accurately capturing the streamline curvature and swirl especially near the substrate.

Reynolds averaging

In Reynolds average turbulence modeling, the solution variables are disintegrated into a mean (time averaged) and a fluctuating component. For instance, flow velocity based on this approach is written as,

$$u_i = \bar{u}_i + u_i' \tag{2-8}$$

where $\bar{u}_i$ and $\acute{u}_i$ are the mean and fluctuating components of the velocity respectively *(i* =1, 2, 3).

Substituting the flow variables into the instantaneous continuity and momentum equations and tacking the time average will lead to Reynolds-averaged Navier-Stokes (RANS) equations as shown below [25].

$$\frac{\partial \rho}{\partial t} + \frac{\partial}{\partial x_i}\left(\rho u_i\right) = 0 \tag{2-9}$$

$$\frac{\partial}{\partial t}\left(\rho u_i\right) + \frac{\partial}{\partial x_j}\left(\rho u_i u_j\right) = -\frac{\partial P}{\partial x_i} + \frac{\partial}{\partial x_j}\left[\mu\left(\frac{\partial u_i}{\partial x_j} + \frac{\partial u_j}{\partial x_i} - \frac{2}{3}\delta_{ij}\frac{\partial u_l}{\partial x_l}\right)\right] + \frac{\partial}{\partial x_j}\left(-\rho\overline{u_i' u_j'}\right) \tag{2-10}$$

where

- $\frac{\partial}{\partial t}(\rho u_i)$ = Unsteady term
- $\frac{\partial}{\partial x_j}(\rho u_i u_j)$ = Advection term
- $\frac{\partial P}{\partial x_i}$ = Pressure gradient term
- $\frac{\partial}{\partial x_j}\left[\mu\left(\frac{\partial u_i}{\partial x_j}+\frac{\partial u_j}{\partial x_i}-\frac{2}{3}\delta_{ij}\frac{\partial u_l}{\partial x_l}\right)\right]$ = Diffusion term

The term$(-\rho\overline{\acute{u}_i\acute{u}_j})$, is called Reynolds shear stresses and closing above equations requires proper modeling of these terms. In one common approach the Reynolds stresses are related to the velocity gradients by using the Boussinesq approximation as follows,

$$-\rho\overline{u_i'u_j'}=\mu_t\left(\frac{\partial u_i}{\partial x_j}+\frac{\partial u_j}{\partial x_i}\right)-\frac{2}{3}\left(\rho k+\frac{\partial u_k}{\partial x_k}\right)\delta_{ij} \tag{2-11}$$

where k is turbulence kinetic energy, μ_t is the turbulent eddy viscosity, and δ is Dirac delta function [25].This approach is used in k-ε and k-ω models to model the Reynolds stresses. An alternative approach is given in Reynolds stress model (RSM) in which, instead of relying on eddy-viscosity hypothesis, the Reynolds stresses terms together with an equation for the dissipation rate are solved in order to close the Reynolds-averaged Navier-Stokes equations.

Reynolds stress model

Instead of utilizing the Boussinesq hypothesis, there is an alternative approach called Reynolds stress model (RSM) in which each of the terms in Reynolds stress tensor is solved by means of a transport equation. Therefore, in a 3D case using RSM turbulence model, seven additional transport equations must be solved. The exact transport equation for Reynolds stresses in RSM model is given as below [25].

$$\underbrace{\frac{\partial}{\partial}\left(\rho\overline{u_i'u_j'}\right)}_{1}+\underbrace{\frac{\partial}{\partial}\left(\rho u_k\overline{u_i'u_j'}\right)}_{2}=\underbrace{-\frac{\partial}{\partial}\left(\rho\overline{u_i'u_j'u_k'}+\overline{p'\left(\delta_{kj}u_i'+\delta_{ik}u_j'\right)}\right)}_{3}$$
$$+\underbrace{\frac{\partial}{\partial}\left(\mu\frac{\partial}{\partial}\left(\overline{u_i'u_j'}\right)\right)}_{4}-\underbrace{\rho\left(\overline{u_i'u_k'}\frac{\partial u_j}{\partial}+\overline{u_j'u_k'}\frac{\partial u_i}{\partial}\right)}_{5} \qquad (2\text{-}12)$$
$$+\underbrace{\overline{p'\left(\frac{\partial u_i'}{\partial x_j}+\frac{\partial u_j'}{\partial x_i}\right)}}_{6}-\underbrace{2\mu\left(\overline{\frac{\partial u_i'}{\partial x_k}\frac{\partial u_j'}{\partial x_k}}\right)}_{7}$$

where

1) $\frac{\partial}{\partial t}\left(\rho\overline{u_i'u_j'}\right)=$ Local Time Derivative

2) $\frac{\partial}{\partial x_k}\left(\rho u_k\overline{u_i'u_j'}\right)=$ Convection

3) $\frac{\partial}{\partial x_k}\left(\rho\overline{u_i'u_j'u_k'}+\overline{p'\left(\delta_{kj}u_i'+\delta_{ik}u_j'\right)}\right)=$ Turbulent Diffusion

4) $\frac{\partial}{\partial x_k}\left(\mu\frac{\partial}{\partial x_k}\left(\overline{u_i'u_j'}\right)\right)=$ Molecular Diffusion

5) $\rho\left(\overline{u_i'u_k'}\frac{\partial u_j}{\partial x_k}+\overline{u_j'u_k'}\frac{\partial u_i}{\partial x_k}\right)=$ Stress Production

6) $\overline{p'\left(\frac{\partial u_i'}{\partial x_j}+\frac{\partial u_j'}{\partial x_i}\right)}$ = Pressure Strain

7) $2\mu\left(\overline{\frac{\partial u_i'}{\partial x_k}\frac{\partial u_j'}{\partial x_k}}\right)$ = Viscous Dissipation

Turbulent kinetic energy in this model is obtained from:

$$k=\frac{1}{2}\overline{u_i'u_i'} \tag{2-13}$$

The dissipation tensor, ε_{ij} is then modeled by:

$$\varepsilon_{ij}=\frac{2}{3}\delta_{ij}(\rho\varepsilon+Y_M) \tag{2-14}$$

where

$$Y_M=2\rho\varepsilon M_t^2 \tag{2-15}$$

M_t is the turbulent Mach number and is defined as:

$$M_t=\sqrt{\frac{k}{a^2}} \tag{2-16}$$

The scalar dissipation rate, ε, is computed with a transport model similar to the one used in k-ε model [25].

$$\frac{\partial}{\partial t}(\rho\varepsilon)+\frac{\partial}{\partial x_i}(\rho\varepsilon u_i)=\frac{\partial}{\partial x_j}\left[\left(\mu+\frac{\mu_t}{\sigma_\varepsilon}\right)\frac{\partial\varepsilon}{\partial x_j}\right]C_{\varepsilon 1}\frac{1}{2}P_{ii}\frac{\varepsilon}{k}-C_{\varepsilon 2}\rho\frac{\varepsilon^2}{k} \tag{2-17}$$

In the above equation, $\sigma_\varepsilon = 1.0$, $C_{\varepsilon 1} = 1.44$, and $C_{\varepsilon 2} = 1.92$. P_{ii} is the stress production term in the Reynolds stress equation.

Thus the turbulent eddy-viscosity is computed from the equation below.

$$\mu_t = \rho C_\mu \frac{k^2}{\varepsilon} \tag{2-18}$$

where $C_\mu = 0.09$ [25].

2.1.3. Near wall treatment

Inclusion of solid walls has significant effect on flows and their turbulence behavior in the computational domain. Solution variables will experience large gradients near walls' region which gives a rise to the turbulence production. Therefore, a proper representation of the flow near the wall is needed to maintain the accuracy of the solution.

Experiments show that in the vicinity of the wall, flow can be divided to three different layers as shown as in Figure 2.2 [28]

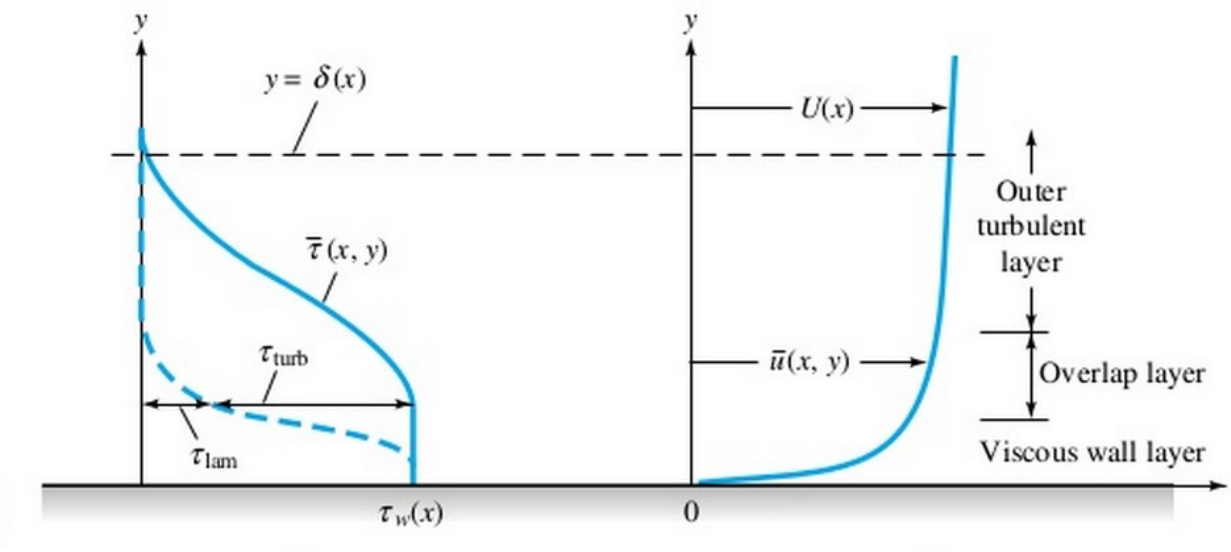

Figure 2.1 Velocity and shear distribution near the wall [28]

Molecular viscosity and viscous shear are dominant adjacent to the wall in the viscous wall layer and flow is almost laminar. Further away from the wall in the turbulent layer, turbulent shear plays a major role. There is a transition layer between viscous sublayer and fully turbulent layer in which the effects of both molecular and turbulent viscosities are important. [28].

Wall functions

There are two main approaches to model near wall region. In one approach, viscous sublayer is resolved all the way to the wall. This needs sufficiently fine mesh ($y^+ = 1$) near the wall which can impose large computational requirement. The second approach which is chosen for this study relies on using semi empirical equation to connect the wall region to the turbulent outer layer.

The law of the wall for the mean velocity is used as follows.

$$U^* = \frac{1}{\kappa}\ln\left(Ey^*\right) \qquad y^* > 11.225 \qquad (2\text{-}19)$$

$$U^* = y^* \qquad y^* < 11.225 \qquad (2\text{-}20)$$

Where U^* is the dimensionless velocity and y^* the distance of the element from the wall are calculated as follows [25].

$$U^* \equiv \frac{U_P C_\mu^{\frac{1}{4}} k_P^{\frac{1}{2}}}{\mu} \qquad (2\text{-}21)$$

$$y^* \equiv \frac{\rho C_\mu^{\frac{1}{4}} k_P^{\frac{1}{2}} y_P}{\mu} \qquad (2\text{-}22)$$

where,

$\kappa =$ Von Karman constant (=0.4187).

E = Empirical constant (=9.793).

U_P = Mean velocity of the fluid at the adjacent cell centroid.

k_P = Turbulent kinetic energy at the wall-adjacent cell centroid.

y_P = Distance from the centroid of the wall-adjacent cell to the wall.

Also a logarithmic law for the mean temperature based on Reynold's analogy between momentum and energy transport is employed here as follows.

$$T^* \equiv \frac{(T_W - T_P)\rho c_p C_\mu^{\frac{1}{4}} k_P^{\frac{1}{2}}}{\dot{q}} = Pry^* \qquad y^* < y_T^* \tag{2-23}$$

$$T^* \equiv \frac{(T_W - T_P)\rho c_p C_\mu^{\frac{1}{4}} k_P^{\frac{1}{2}}}{\dot{q}} = Pr_t\left[\frac{1}{\kappa}\ln\left(Ey^*\right) + P\right] \qquad y^* > y_T^* \tag{2-24}$$

where P is computed from the below formula

$$P = 9.24\left[\left(\frac{Pr}{Pr_t}\right)^{\frac{3}{4}} - 1\right]\left[1 + 0.28e^{\frac{-0.007Pr}{Pr_t}}\right] \tag{2-25}$$

Two extra terms are added to the right hand side of equations 2-23 and 2-24 for the compressible flow calculations [25]. In the above equations,

c_p = Specific heat of fluid

$\dot{q}$= Wall heat flux.

T_P = Temperature at the wall-adjacent cell centroid.

T_W = Temperature at the wall.

Pr = Molecular Prandtl number.

Pr_t = Turbulent Prandtl number (0.85 at the wall).

2.1.4. Numerical technique

The governing integral equations for conservation of mass, momentum, energy or any other scalar are solved in ANSYS-Fluent by means of a control volume based technique. In this technique, first by using a computational mesh, the domain is divided into discrete control volumes. In the next step, algebraic equations are constructed in order to find unknown variables (pressure, velocity, etc.) by integrating the governing equations over the control volumes. Then the discretized equations are linearized and solution to the resulting linear equation system is sought [25]. A Pressure-based solver (SIMPLE scheme) is chosen for pressure-velocity coupling in this work. In the pressure-based method by solving the pressure equation, mass conservation of the velocity field is achieved. By using the momentum and continuity equations, the pressure equation is constructed in such a way that the velocity corrected by pressure satisfies the continuity equation. Figure 2.1 shows a solution loop for segregated pressure-based algorithm in which governing equations are solved sequentially [25]. The second order upwind differencing scheme is used to determining the flow values at the cell faces.

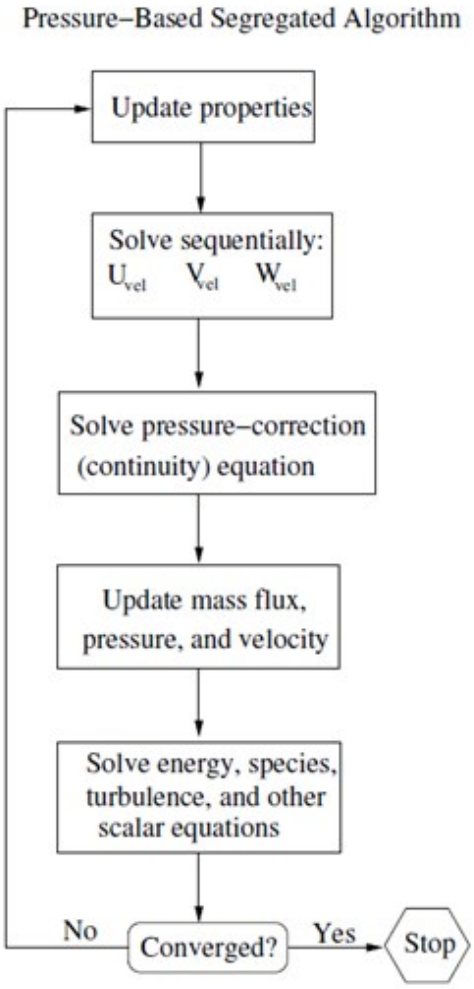

Figure 2.2 Solution loop for the Pressure-based segregated solver [25]

2.2. Dispersed phase

In this step, after the solution to the continuous phase is converged, solution to disperse phase is obtained by injecting droplets/particles into the calculated flow field that can exchange mass, momentum and energy with the continuous phase.

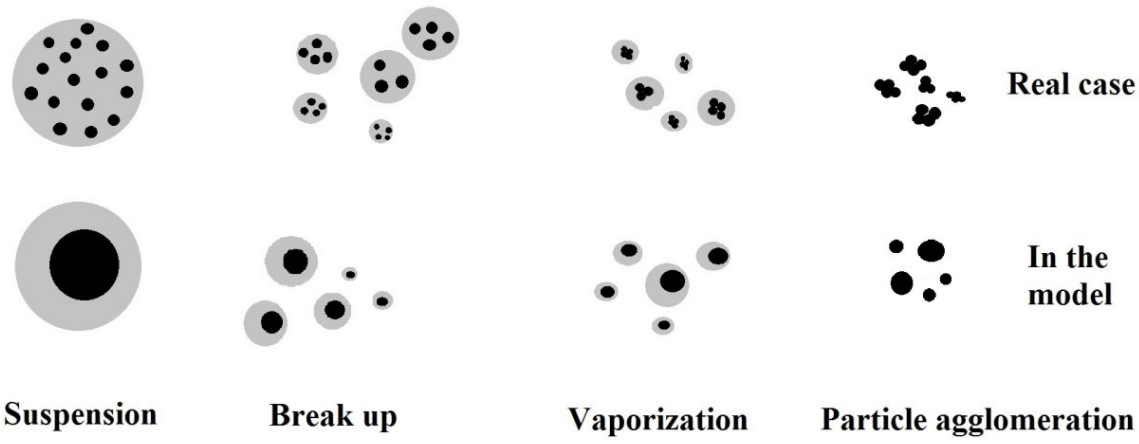

Figure 2.3 Schematic of the phenomena involved in suspension droplet evolution in a real and a model case [12]

In this approach, it is assumed that the dispersed phase has a low volume fraction compared to the continuous one so that the particle-particle interaction can be neglected.

In this study in a way similar to [14] as is shown in the Figure 2.3, suspension is modeled as a multi-component droplet carrying properties of zirconia and ethanol as the base solvent. These droplets undergo break up and evaporation and each newly generated droplet has the same concentration until ethanol is fully evaporated. The surface tension of the suspension is assumed to be 20% more than that of the pure alcohol as far as the break up is dominant [29]. The specific heat of the zirconia particles during melting is calculated from equation 2-26,

$$C_p \times \Delta T = H_f \tag{2-26}$$

where in 2-26, C_p, is the particle specific heat, and H_f, is the enthalpy of fusion of the particle.

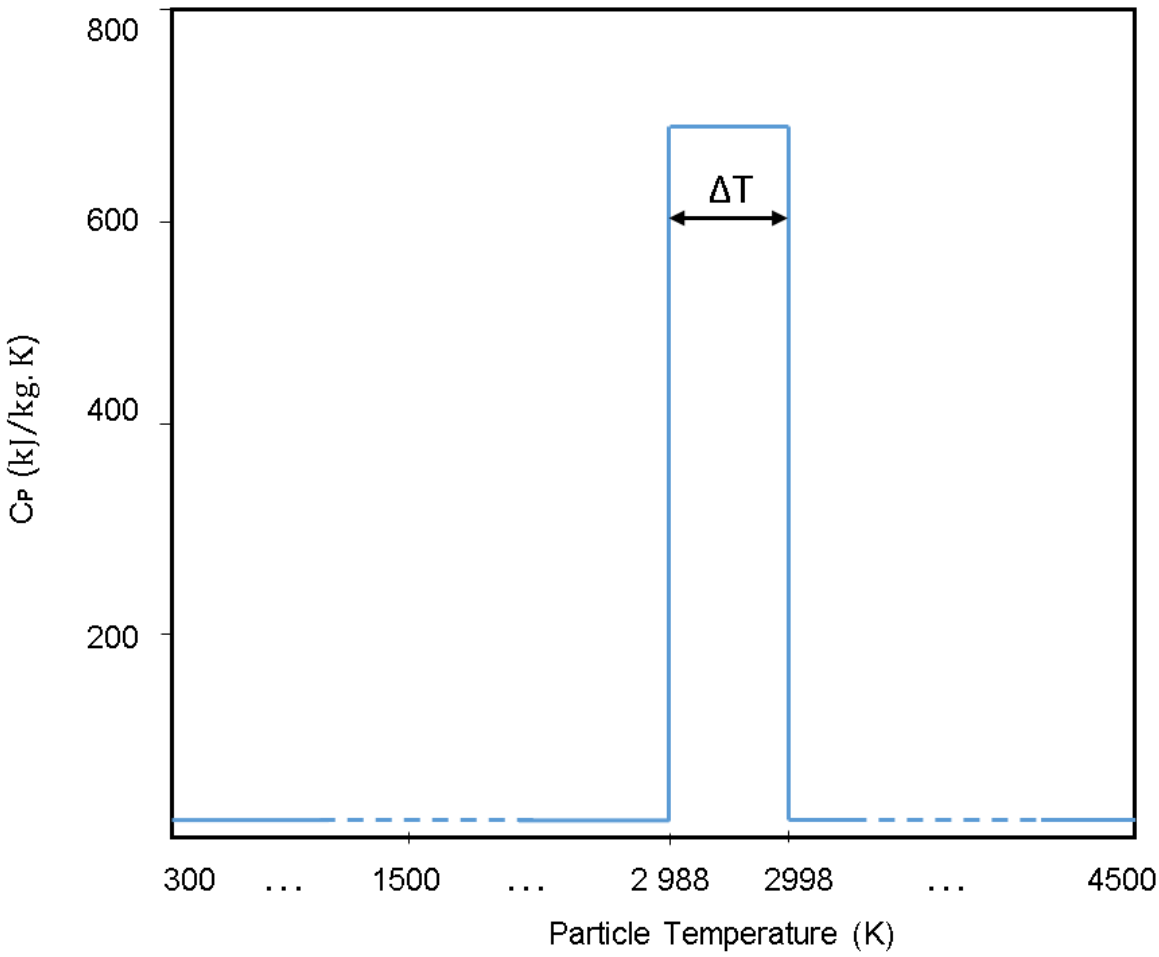

Figure 2.4 Variation of the particles specific heat as a function of temperature.

In order to model melting of the particles, the heat of fusion of the zirconia particles was embedded in its specific heat as shown in Figure 2.4, where in equation 2-26 ΔT is assumed to be 10 °C. In this study, the effect of radiative heat transfer is neglected. Moreover, due to the small sized particles used in SPS, temperature gradients are neglected within the particles and therefore lumped capacitance assumption is made here (Bi<0.1). Thus, particles experience uniform temperature distribution at each integration step.

Finally, by using the stochastic tracking model, the effect of turbulence on dispersion of the particles has been investigated. This is accomplished by including the instantaneous turbulent velocity fluctuation on particle trajectories.

2.2.1. Particle dynamics

Writing a force balance on a particle in Lagrangian reference frame will lead to equation 2-27.

$$\frac{d\vec{u}_p}{dt} = F_D\left(\vec{u} - \vec{u}_p\right) + \frac{\vec{g}\left(\rho_p - \rho\right)}{\rho_p} \tag{2-27}$$

In equation 2-27, $F_D\left(\vec{u} - \vec{u}_p\right)$ is the drag force per particle's mass which can be obtained from:

$$F_D = \frac{18\mu C_D Re}{\rho_p d_p^2 24} \tag{2-28}$$

where in 2-27 and 2-28:

$\vec{u}$ = Continues phase velocity.

$\vec{u}_p$ = Particle velocity.

ρ_p = Density of the particle.

d_p = Diameter of the particle.

The Reynolds number used in 2-28 is based on the relative velocity between the fluid phase and the dispersed phase.

$$Re = \frac{\rho d_p \left(\vec{i} \cdot \vec{} - \vec{} _p \right)}{\mu} \tag{2-29}$$

The drag coefficient used in equation 2.28 is obtained from the correlation proposed by Morsi and Alexander [30],

$$C_D = a_1 + \frac{a_2}{Re} + \frac{a_3}{Re^2} \tag{2-30}$$

where a_1, a_2 and a_3 are constants and a function of Reynolds number as in [30]. Consequently, particle's trajectory is then calculated by integrating equation 2-27.

2.2.2. Particle heat and mass transfer

The energy equation for a multi component particle is written as follows.

$$m_p c_p \frac{dT}{dt} = hA_p(T_\infty - T_P) + \sum_i \frac{dm_i}{dt}(h_{fg,i}) \tag{2-31}$$

where:

m_p = Mass of the particle (kg)

c_p = Heat capacity of the particle ($\frac{J}{kg.k}$)

A_p= Surface area of the particle (m^2)

T_∞ = Local temperature of the continuous phase (K)

T_P = Particle temperature (K)

h = Convective heat transfer coefficient ($\frac{W}{m^2.K}$)

h_{fg} = Latent heat ($\frac{J}{kg}$)

The convective heat (h) and mass (k_c), transfer coefficients are calculated based on correlations proposed by Ranz and Marshall [31], [32].

$$Nu = \frac{hd_p}{k} = 2.0 + 0.6Re_p^{\frac{1}{2}}Pr^{\frac{1}{3}} \tag{2-32}$$

$$Sh_{AB} = \frac{k_c d_p}{D_{i,m}} = 2.0 + 0.6Re_d^{\frac{1}{2}}Sc^{\frac{1}{3}} \tag{2-33}$$

where

Pr = Prandtl number of the continuous phase ($\frac{c_p \mu}{k}$)

k = Thermal conductivity of continuous phase ($\frac{W}{m.K}$)

k_c = Mass transfer coefficient ($\frac{m}{s}$)

$D_{i,m}$ = Diffusion coefficient of vapor in the bulk ($\frac{m^2}{s}$)

Sc = Schmidt number of continuous phase ($\frac{\mu}{\rho D_{i,m}}$)

The rate of the change of the droplet mass due to the evaporation is calculated from [33].

$$\frac{dm_p}{dt} = k_c A_P \rho_\infty \ln\left(1 + B_m\right) \tag{2-34}$$

In 2-34, B_m is the Spalding number and is calculated as follows [34],

$$B_m = \frac{Y_{i,s} - Y_{i,\infty}}{1 - Y_{i,s}} \tag{2-35}$$

where:

$Y_{i,s}$ = Mass fraction of the vapor at surface

$Y_{i,\infty}$= Mass fraction of the vapor in continuous gas

2.2.3. Droplet break up

Suspension droplets start to break up as they interact with the plasma flow. Since the droplet Weber number when travelling inside the plasma core is in the catastrophic break up regime ($We \sim 300$), droplets are fragmented due to the presence of the Rayleigh-Taylor and Kelvin-Helmholtz instabilities. Therefore, the KHRT break up model which is a combination of Kelvin-Helmholtz waves induced by the aerodynamic forces and Rayleigh-Tylor instabilities due to the acceleration of the newly formed droplets in the flow stream is used to simulate the break up process as shown in the Figure 2.5[2].

[2] Extracted from http://www.math.mtu.edu/~tanner/Research/

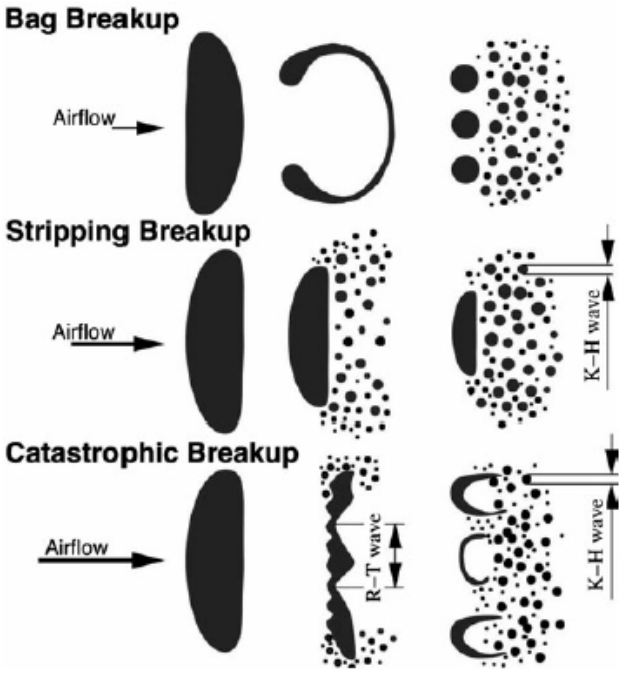

Figure 2.5[2] Various mechanisms for droplet break up

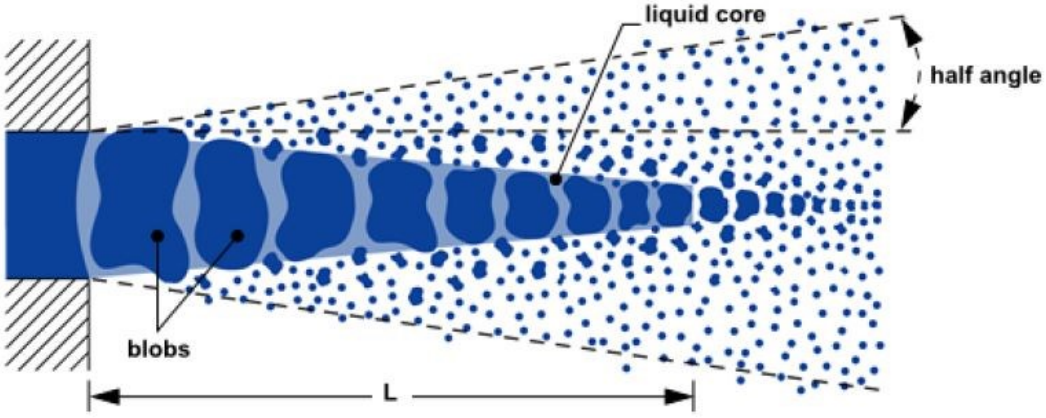

Figure 2.6 Liquid core formation and droplet atomization in the KHRT break up model [25]

KHRT model considers the presence of a liquid core near the nozzle exit region as shown in Figure 2.6. Particles are shed from the original formed droplets and accelerated in the flow as the liquid core diminishes [25].

The wave growth at the droplet surface is calculated according to both of these instabilities. Afterwards, break up happens based on the fastest growing instability on the droplet surface. Inside the liquid core (as shown in Figure 2.6) only the aerodynamic instabilities are considered while outside the liquid core both of the Kelvin-Helmholtz and Rayleigh-Tylor instabilities are present. The details associated with the droplet break up models are described below.

Wave breakup model

In wave break up model, the aerodynamic instabilities are the result of the relative velocity between the injected droplets and the gas flow.

The radius of the newly formed droplets due to the wave propagation is calculated based on the wavelength of the fastest-growing unstable surface wave on the initial parent droplet. In other words,

$$r = B_0 \Lambda \tag{2-36}$$

where B_0 is a model constant set equal to 0.61 based on the work of Reitz [35]. Moreover, the radius of the parent droplet changes according to,

$$\frac{da}{dt} = -\frac{(a-r)}{\tau} \qquad r \le a \tag{2-37}$$

where, τ, is the breakup time given by,

$$\tau = \frac{3.726\ B_1 a}{\Lambda\Omega} \tag{2-38}$$

The maximum growth rate and its corresponding wave length, Ω and Λ are calculated from the following equations.

$$\frac{\Lambda}{a} = 9.02\frac{\left(1+0.45Oh^{0.5}\right)\left(1+0.4Ta^{0.7}\right)}{\left(1+0.87We_2^{1.67}\right)^{0.6}} \tag{2-39}$$

$$\Omega\left(\frac{\rho_1 a^3}{\sigma}\right) = \frac{\left(0.34+0.38We_2^{1.5}\right)}{\left(1+Oh\right)\left(1+1.4Ta^{0.6}\right)} \tag{2-40}$$

In the above equations, *Oh* and *Ta* are the Ohnesorge and Taylor numbers given by equations 2-41 and 2-42 [35].

$$Oh = \frac{\sqrt{We_1}}{Re_1} \tag{2-41}$$

$$Ta = Oh\sqrt{We_2} \tag{2-42}$$

In equation (2-41) Re_1 is the Reynolds number [35],

$$Re_1 = U\frac{a}{\nu_1} \tag{2-43}$$

and a is the liquid jet radius and ν_1 is the dynamic viscosity of liquid. In addition, We_1 and We_2 are the liquid and gas Weber numbers, respectively, given by equations 2-43 and 2-44.

$$We_1 = \rho_1 U^2 \frac{a}{\sigma} \tag{2-44}$$

$$We_2 = \rho_2 U^2 \frac{a}{\sigma} \tag{2-45}$$

In equations (2-43) and (2-44) ρ_1 is the liquid density, ρ_2 is the gas density and U is the relative velocity between liquid and gas.

A new parcel is added to computation when the mass removed from the parent droplet reaches 5% of the initial parcel mass. The new parcel would have the same properties such as temperature, material, position, etc. except for the radius and velocity [25].

Rayleigh-Taylor breakup model

The Rayleigh-Taylor (RT) model is based on wave instabilities formed on the droplet surface induced by the acceleration of the droplet in the flow field. Similar to the Kelvin-Helmholtz model the droplet break up is related to the fastest growing wave frequency (Ω_{RT}) which is computed by,

$$\Omega_{RT} = \sqrt{\frac{2\left(-g_t\left(\rho_p - \rho_g\right)\right)^{\frac{3}{2}}}{3\sqrt{3\sigma}\left(\rho_p - \rho_g\right)}} \tag{2-46}$$

where g_t is the acceleration of droplet in the direction of the droplet motion [25]. The wave number K_{RT}, is calculated by equation 2-47,

$$K_{RT} = \sqrt{\frac{-g_t\left(\rho_p - \rho_g\right)}{3\sigma}} \tag{2-47}$$

Droplet break up happens once the RT waves grow for a time greater than the breakup time, τ_{RT},

$$\tau_{RT} = \frac{C_\tau}{\Omega_{RT}} \tag{2-48}$$

C_τ is the Rayleigh-Taylor break up time constant equals to the value of 0.5. Until the predicted wave length is smaller than the local droplet diameter, the wave growth is tracked. The radius of local child droplets is calculated according to [25],

$$r_c = \frac{\pi\ C_{RT}}{K_{RT}} \tag{2-49}$$

where C_{RT} is the break up radius constant with a default value of 1.

2.3. Geometry and boundary conditions

The simulated plasma torch is a 3MB Oerlikon-Metco Gun with a 20 mm long anode and a 6mm diameter exit nozzle. A constant volumetric heat source located inside the torch is added in the energy equation to account for the plasma heat generation. This energy source is calculated from:

$$p''' = \frac{\eta_t EI}{V} \tag{2-50}$$

where $E,\ I,\ V, \eta_t$ are arc voltage, current, anode volume and thermal efficiency, respectively. The gun thermal efficiency is assumed to be 60 % in this study.

Plasma gun operating conditions	
Arc current (A)	500
Arc voltage (V)	65
Ar_H_2 mass flow rate (gr/s)	1.48

.

Table 2.1 Plasma gun operating conditions

Property	Units	Molten Zirconia	Ethanol
Density	kg/m^3	5680	789
Specific heat	$J/kg.K$	1387	2470
Surface Tension	N/m	1.5	0.0223
Melting point	K	2988	…
Boiling point	K	5273	351
Viscosity	m^2/s	6.5×10^{-6}	1.2×10^{-3}
Melting latent heat	J/kg	707×10^3	…
Boiling latent heat	J/kg	9×10^6	855237

Table 2.2 Materials thermo physical properties

The plasma gas is considered as a mixture of Argon and Hydrogen (10% volume fraction), and the plasma gun operating conditions are shown in Table 2.1.

At the inlet, boundary conditions are set as mass flow rate. In addition, turbulence at the inlet is incorporated by turbulence intensity (4.5%) and hydraulic diameter. The temperature at the torch walls is fixed at 300 K due to the effect of water cooling around it.For the side and outlet boundaries pressure inlet and pressure outlet conditions are used

The aim of this study is to investigate the effect of obstruction of flat and curved substrates on the gas flow and particle characteristics. To do so, a flat substrate with dimensions of $25\times25\times2$ mm^3 and an 80 mm long cylinder with a diameter of 25 mm (Figure 2.7) representing the curved substrate are used.

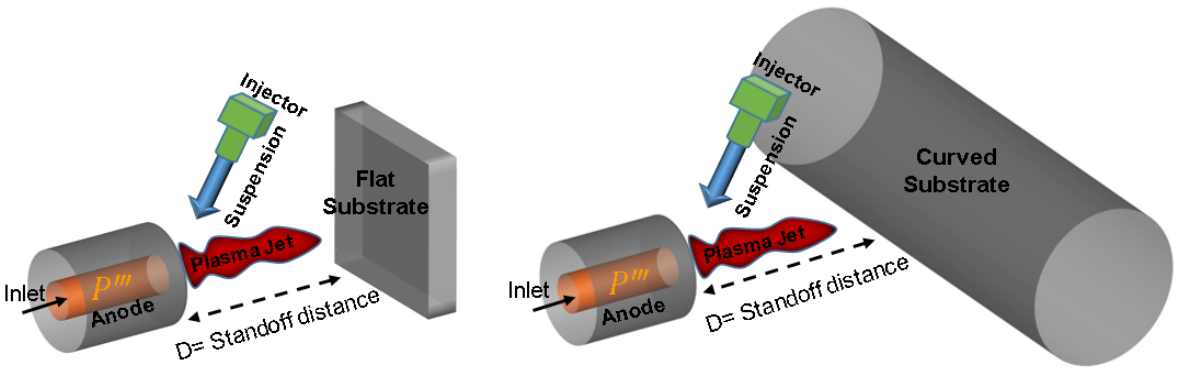

Figure 2.7 The schematic of plasma flow and substrate configuration (flat and curved substrates)

A fixed wall temperature of 700 K [15] for both substrates is applied since the interaction time between the gas flow and the substrate is insignificant. At the solid walls, standard wall functions are used to predict the thermal and velocity boundary layers. Moreover, it is assumed that particles colliding with the substrates stick to the surface. The thermo-physical properties of particle/droplet materials are presented in Table 2.2. An example of

computational domain for the case of cylindrical substrate is shown in Figure. 2.8. The computational domain contains 800,000 hexahedral cells which are locally refined in the plasma core area to capture large plasma temperature and velocity gradients.

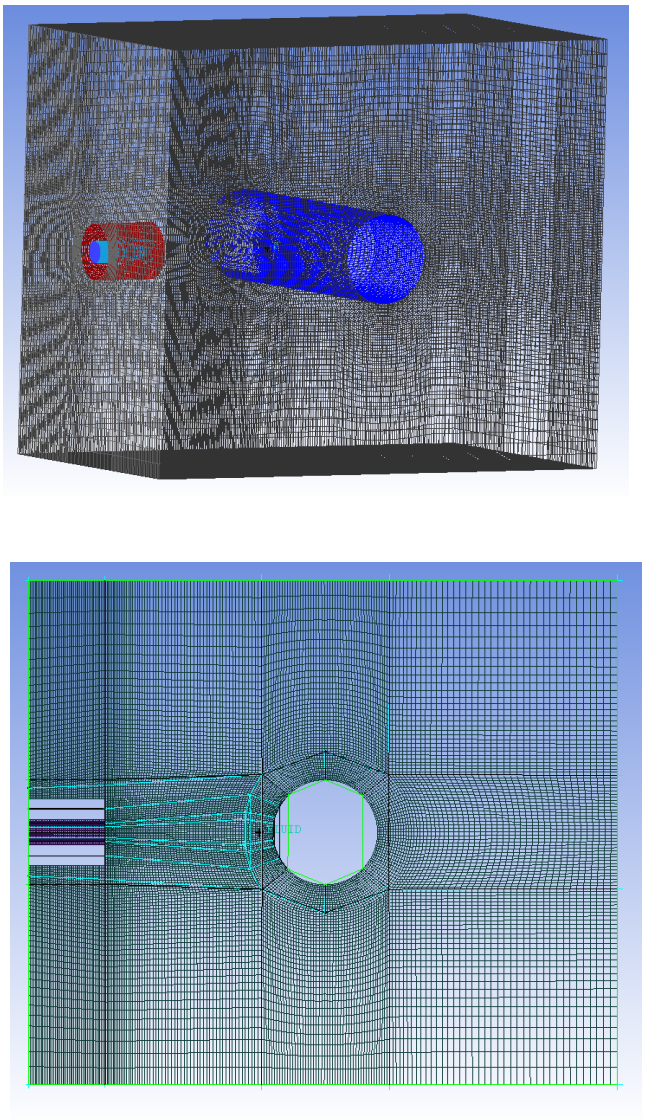

Figure 2.8 Computational mesh and geometry

3. Results

In this chapter

In this chapter, numerical results for continuous and disperse phases with and without the inclusion of the substrates are presented. Effect of changing numerous factors such as substrate standoff distance, curvature and suspension mass flow rate on in-flight particle characteristics are discussed.

Since the level of the solution convergence can be determined by the residual values, throughout this study the required residual value is set to less than 10^{-6} for the energy equation and 10^{-5} for the other equations. Moreover, special attention was paid so that an overall balance for the momentum, energy, mass and other scalars are achieved throughout the domain.

3.1. Gas flow modeling

3.1.1. Free jet

In order to simulate SPS process, first a free jet model without the inclusion of substrate is required. A free jet is categorized by three different zones as illustrated in Figure 3.1. The first zone is called potential core where the velocity of the jet is the same as the velocity at the nozzle exit and remains constant within this zone. Parameters such as turbulence intensity or velocity distribution can affect the length of potential core which may extend by 6-7 diameters of the jet [36]. The presence of shear stresses in the second zone (developing zone) leads to the turbulence generation at the jet boundary and consequently enhances mixing of the jet with the surrounding gas and decelerate the flow. In the last zone (fully developed zone), velocity is considered in a fully developed condition. Figure 3.2 (a) and (b) show the contours of plasma temperature and velocity at the symmetry plane. Figure 3.2 (a) shows a high temperature plasma core exhausting in to atmospheric air at 300 K. Plasma gas is generated by heating up the incoming gas flowing through the embedded source inside the torch. Along the jet centerline, plasma gas starts to cool down due to the mixing of the high temperature plasma with the

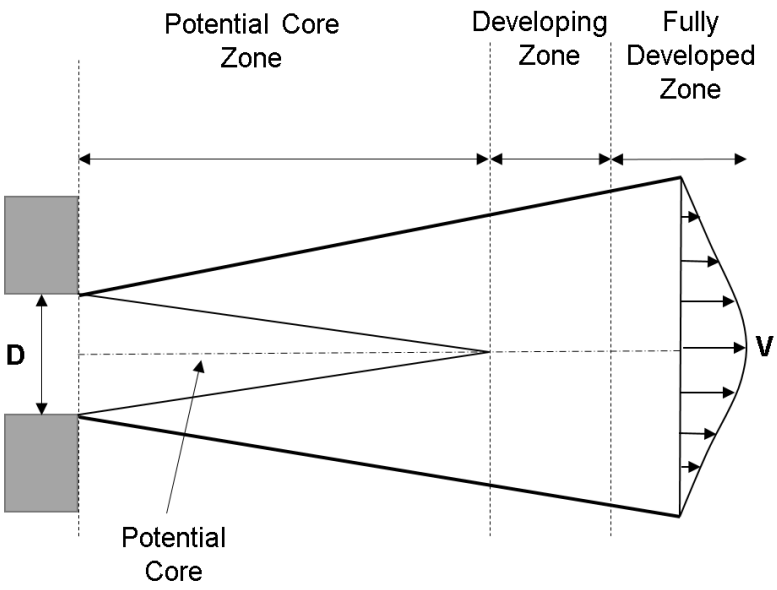

Figure 3.1 Zones involved in a free jet

(a)

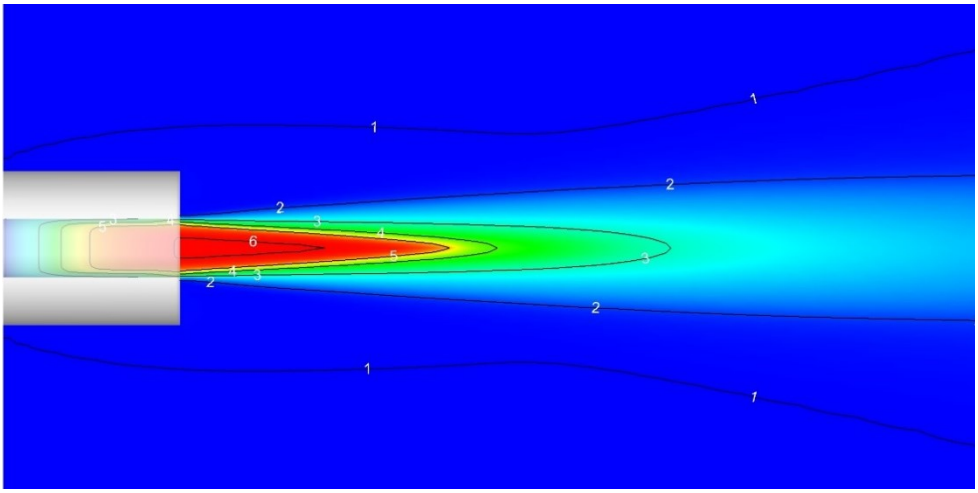

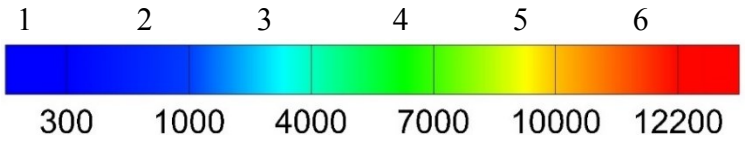

Gas Temperature (K)

(b)

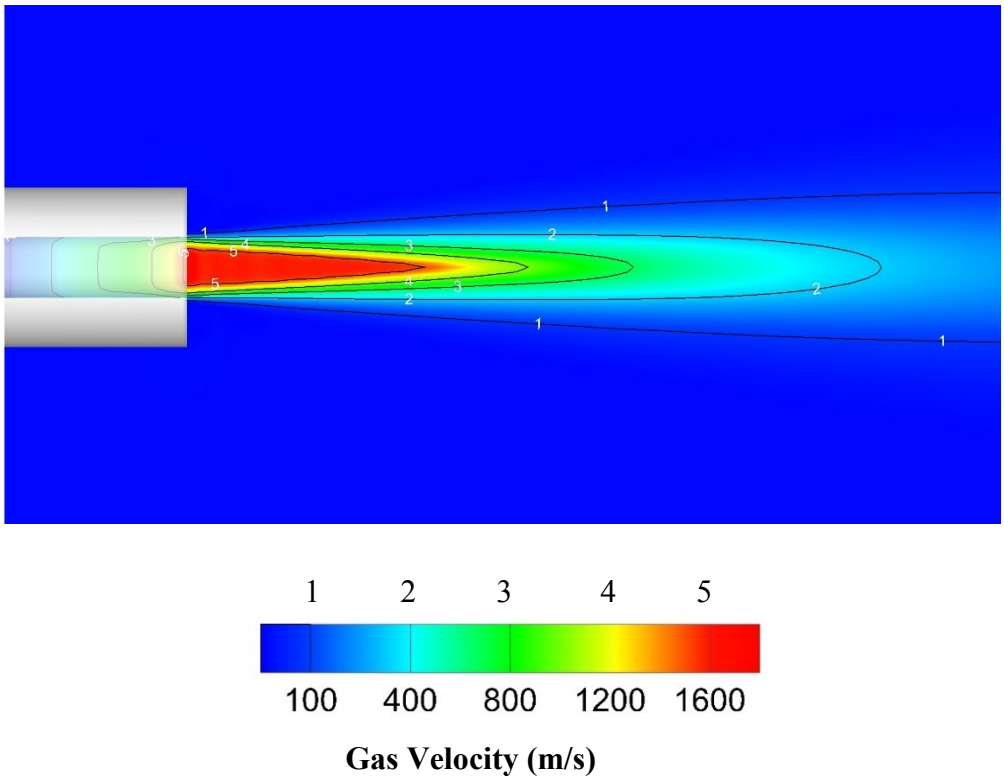

Figure 3.2 Plasma gas (a) temperature and (b) velocity contours

surrounding cold air. Figure 3.2 (b) shows the deceleration of the high velocity plasma gas along the centerline as a result of the presence of the shear stress and mixing of the exhausting high velocity jet with the surrounding air. Furthermore, in order to validate the plasma flow model, the result of this study is compared with the numerical study in [15] which is referred to as the stationary case and also the experimental work of [26] and [27]. In [17], the authors used the modified k-ε classical turbulence model proposed by Bolot et al. [10] to model the plasma flow. The experiment in [26] is based on using the spectroscopic measurements for the highest temperature and enthalpy probe for the lowest ones. In addition in [27], velocity was measured by plasma light fluctuation measurements. Figures 3.3 and 3.4 show the evolution of temperature and velocity of the plasma gas along the torch axis which is in good agreement with numerical and experimental works

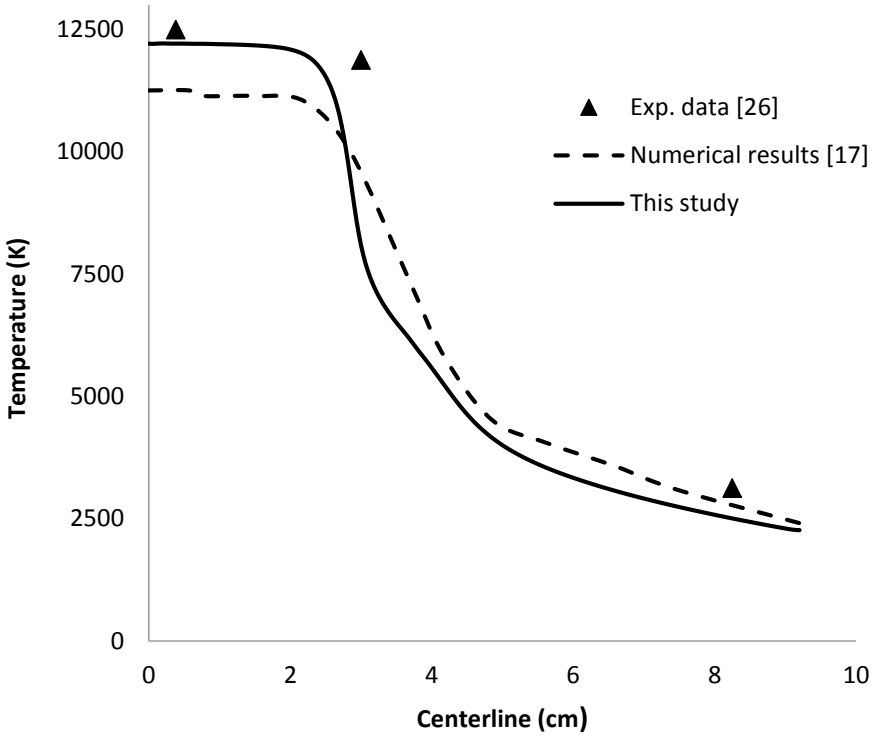

Figure 3.3 Plasma temperature evolution along the centerline

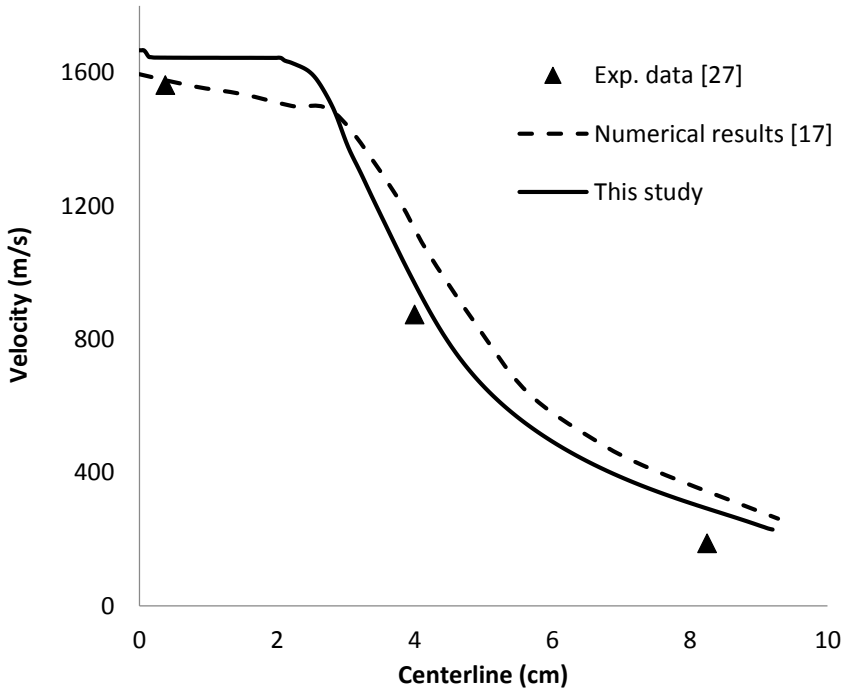

Figure 3.4 Plasma axial velocity along the centerline

mentioned above. The difference between the thermal efficiency considered in this work (60%) and the work of [17] (50%) is assumed to be the reason for maximum temperature discrepancies as it can be seen in Figure 3.3.

3.1.2 Mesh dependency test

In order to examine the sensibility of the solution to the grid size, a grid refinement test has been carried out in this section. This test is performed only for the continuous phase without the presence of a substrate. Two levels of grid size are chosen for this study, a coarse grid with a total of 502,604 elements and a fine grid with a total element number of 3,920,312 in which the number of nodes in each coordinate is roughly doubled. Figure 3.5 shows the solutions for the evolution of velocity and temperature of the free stream along the centerline for these two cases. As it is apparent from Figure 3.5, mesh refinement has not resulted in significant change between the two solutions. The largest difference between the solutions of these two grids is less than 4 % in the worst case condition. Therefore, because of the large computational time and cost related to the fine grid, the coarse grid is used in this study.

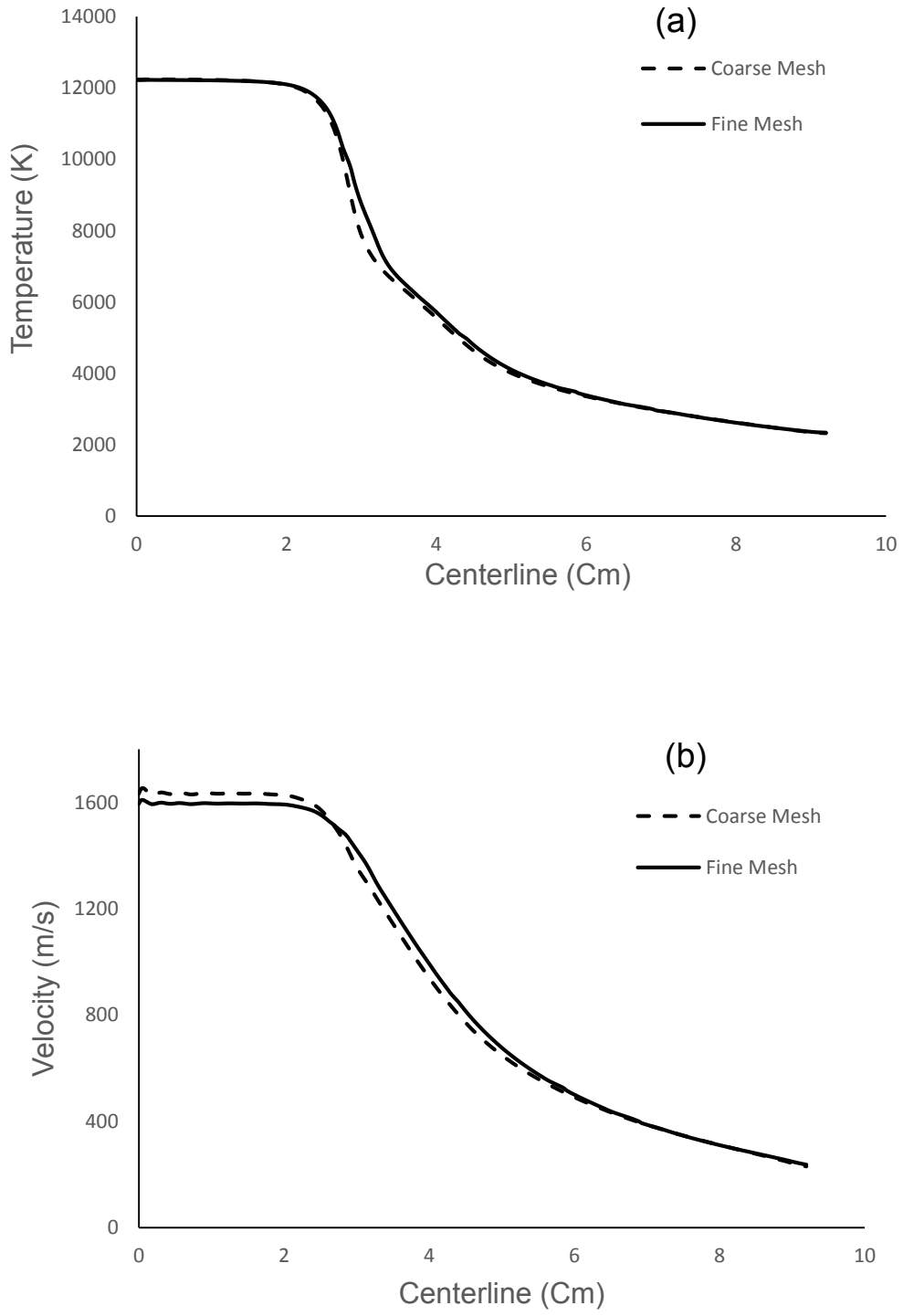

Figure 3.5 Effect of the grid refinement on (a) temperature and (b) velocity of the free jet.

3.1.3. Flat substrate

The focus of this study is to investigate the effect of the substrate and its curvature on in-flight particles trajectories especially at the vicinity of the substrate. To do so, in the first step, the effect of obstruction of a flat substrate at different standoff distances of 4 and 6 cm (D = 4 cm, D = 6 cm) on plasma gas flow and in-flight particle trajectories is investigated. Figure 3.6 shows that as the flow approaches the flat substrate, its axial velocity decreases rapidly and forms a region called stagnation region. Eventually, the plasma gas is brought to a complete stop at the stagnation point which leads to a pressure increase in the stagnation region. The gas flow enters the wall jet region after turning and moves in the radial direction. The pressure decreases as the flow accelerates from the stagnation region parallel to the flat substrate to the wall jet region. The evolution of plasma temperature for the flat substrate at two different standoff distances is also evident in Figure 3.7. Figure 3.8 shows the stagnation pressure on the flat substrate as a function of standoff distance. It is evident from Figure 3.8 (a) and (b) that by increasing the standoff distance from D = 4 cm to D = 6 cm, due to flow deceleration, the stagnation pressure has decreased and a weaker stagnation flow region is formed at the vicinity of the flat substrate. Thus, it can be expected that due to the increase in stagnation pressure in the case of shorter standoff distance the particles that are traveling in the plasma fringes are susceptible to these pressure changes.

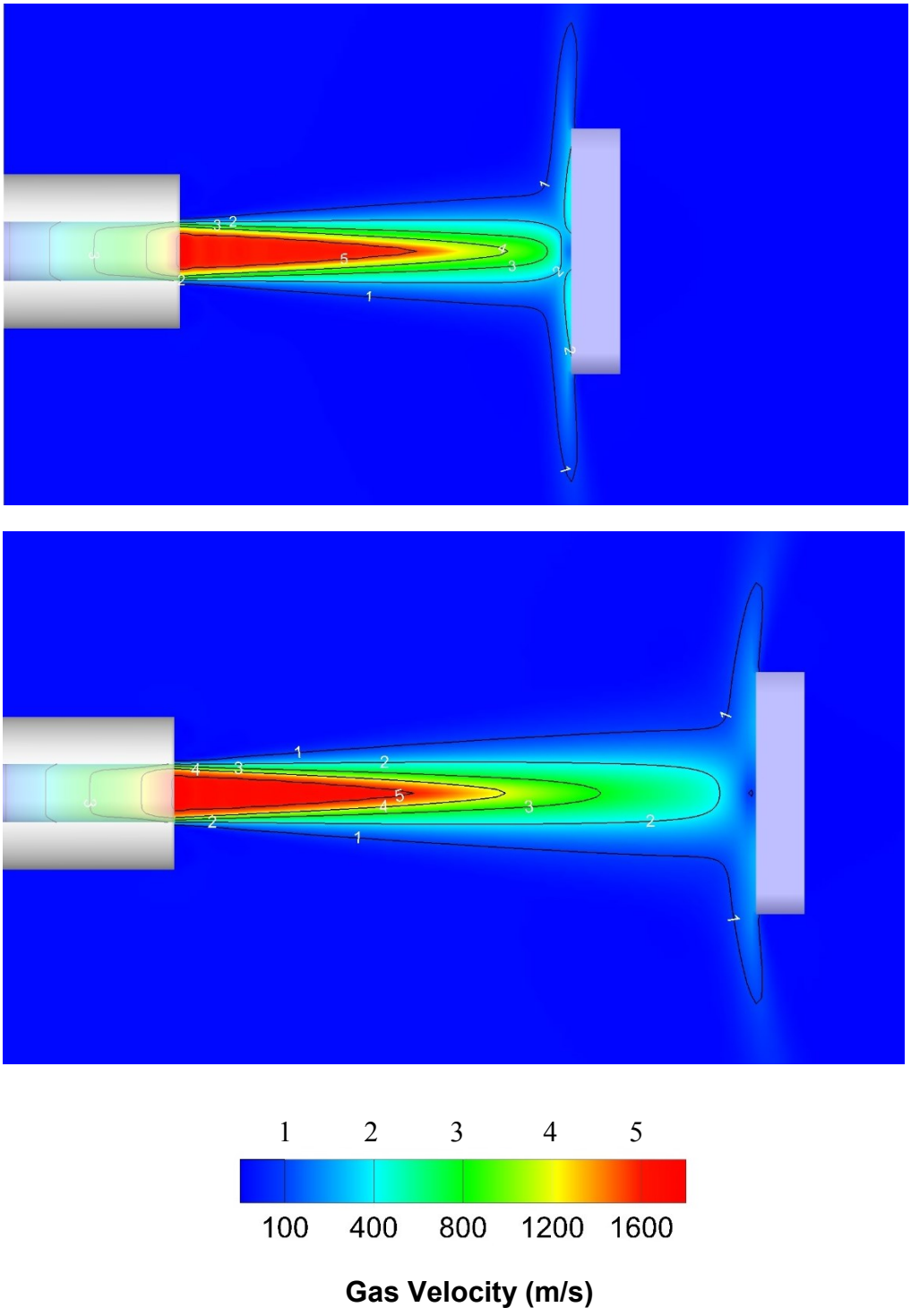

Figure 3.6 Plasma velocity contours for the flat substrate case at standoff distances of D = 4 cm and D = 6 cm.

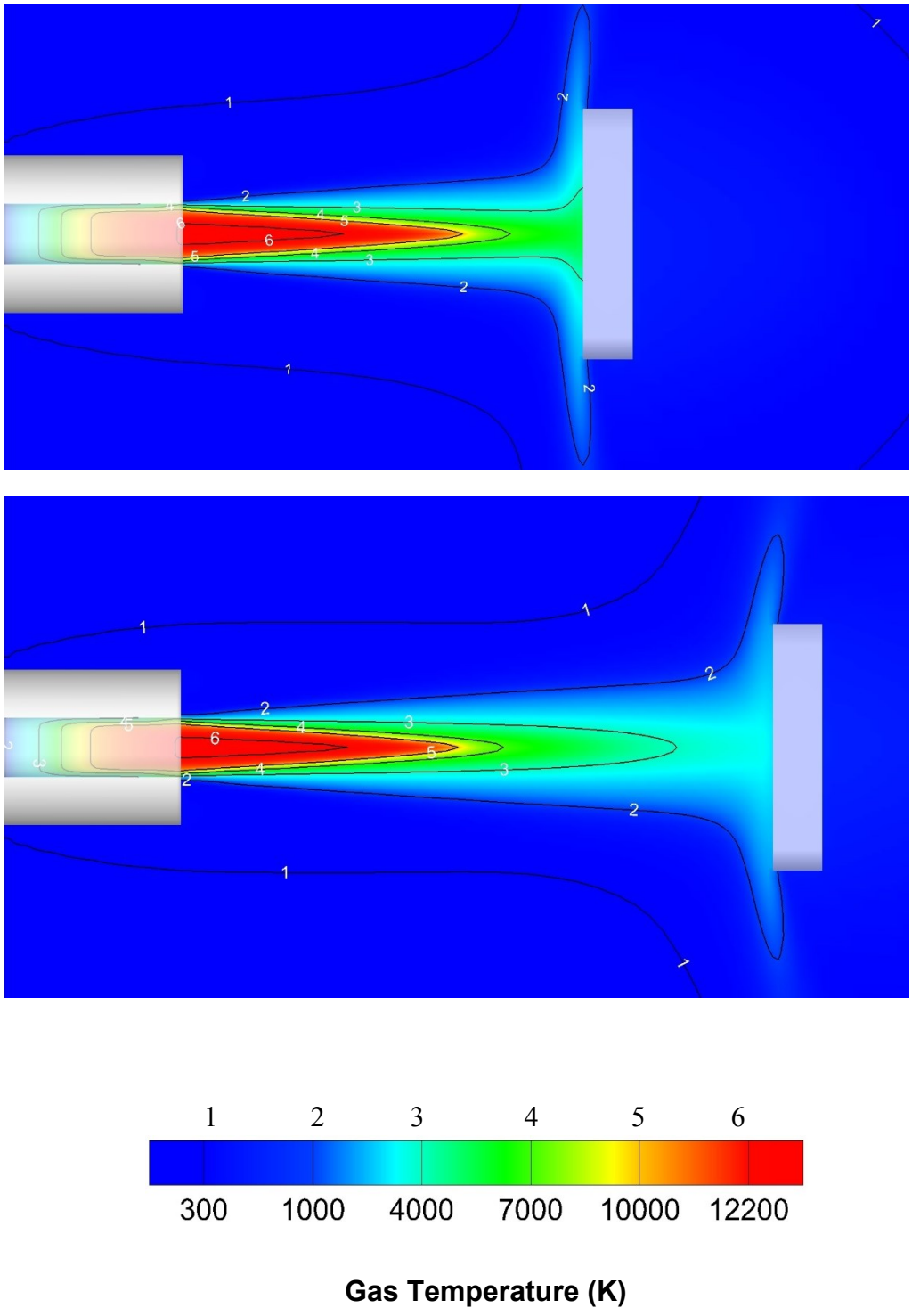

Figure 3.7 Plasma temperature contours for the flat substrate case at standoff distances of D = 4 cm and D = 6 cm.

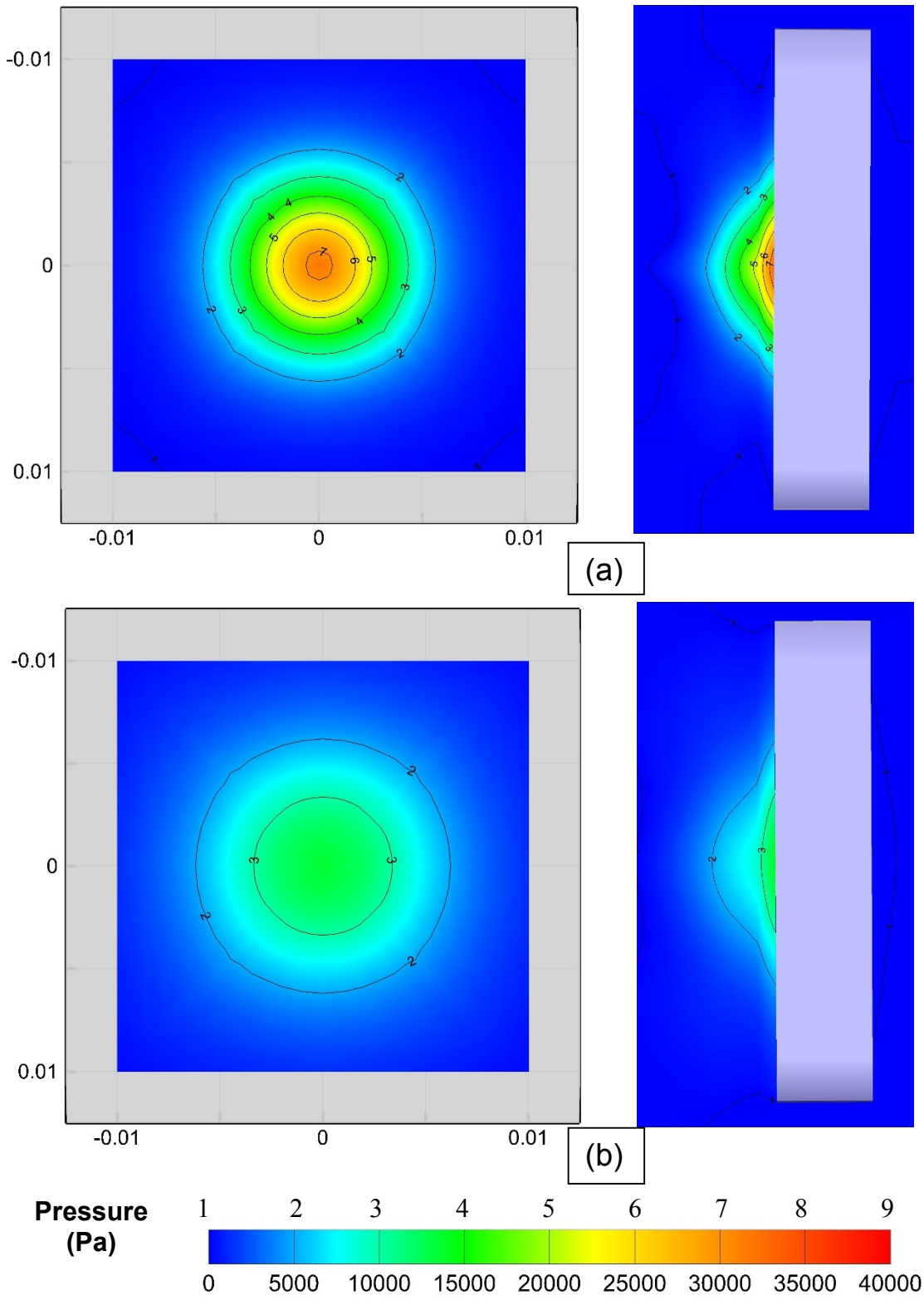

Figure 3.8 Stagnation pressure on a flat substrate located at standoff distances of (a) 4 and (b) 6 cm (dimensions in the above figure are in meters)

3.1.3. Curved substrate

The effect of the substrate curvature on the flow is investigated by obstruction of a cylinder which will be referred to as the curved substrate in this study.

It can be observed from Figure 3.9 that, near the substrate, the flow is diverted along both the circumference and the axis of the cylinder which results in the formation of a wall jet. Figure 3.9 also shows the transition of the free jet region to the stagnation zone near the cylinder and eventually to the wall jet region after turning further downstream of the nozzle. The evolution of the plasma gas temperature impinging on the curved substrate is also shown in Figure 3.10.

The radius of curvature of the cylinder and its effect on the flow pattern is expected to affect the landing location of the particles. Therefore, these phenomena are expected to decrease the deposition efficiency of the curved surface and will be investigated further in this study.

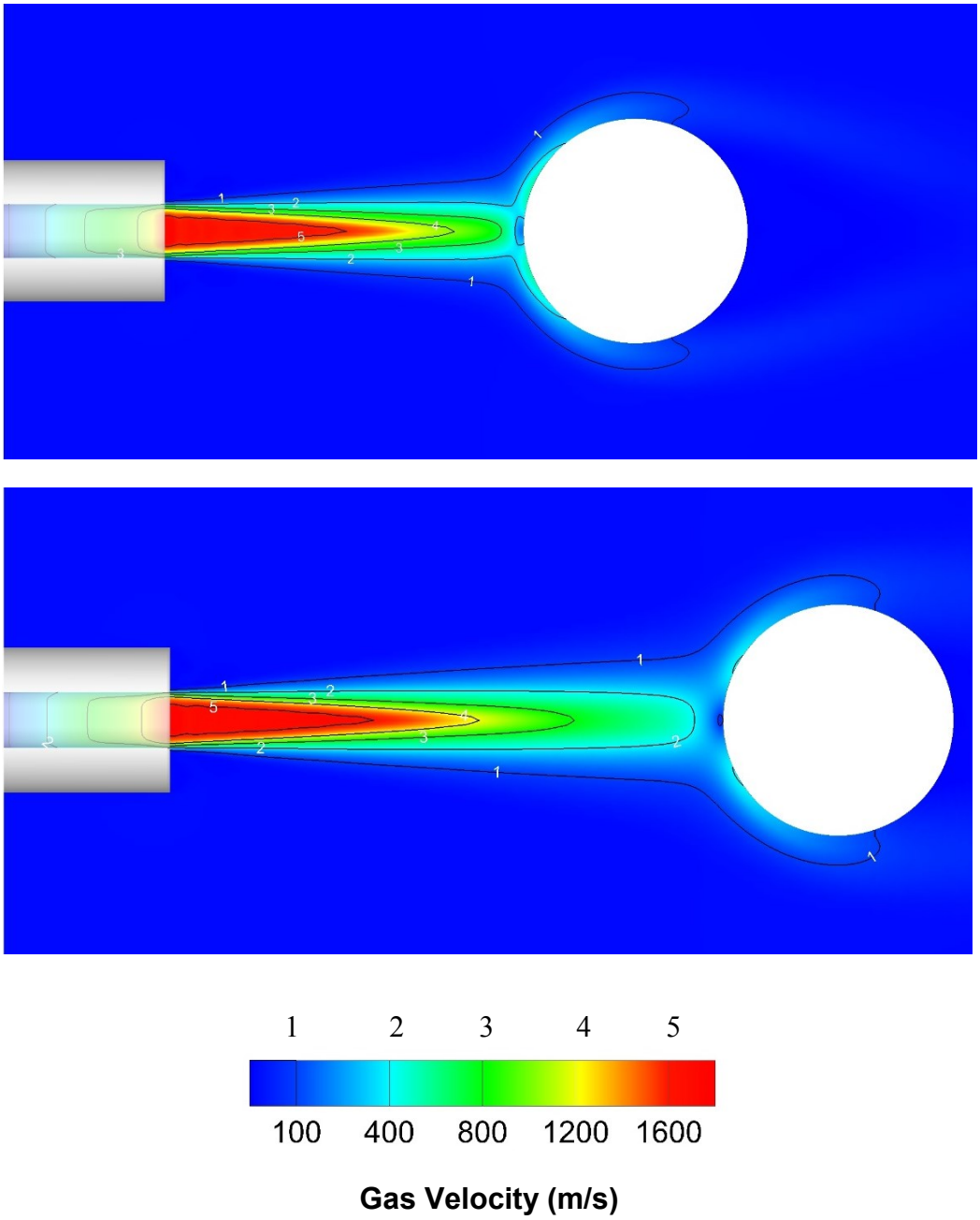

Figure 3.9 Plasma velocity contours for the curved substrates case at standoff distances of D = 4 cm and D = 6 cm

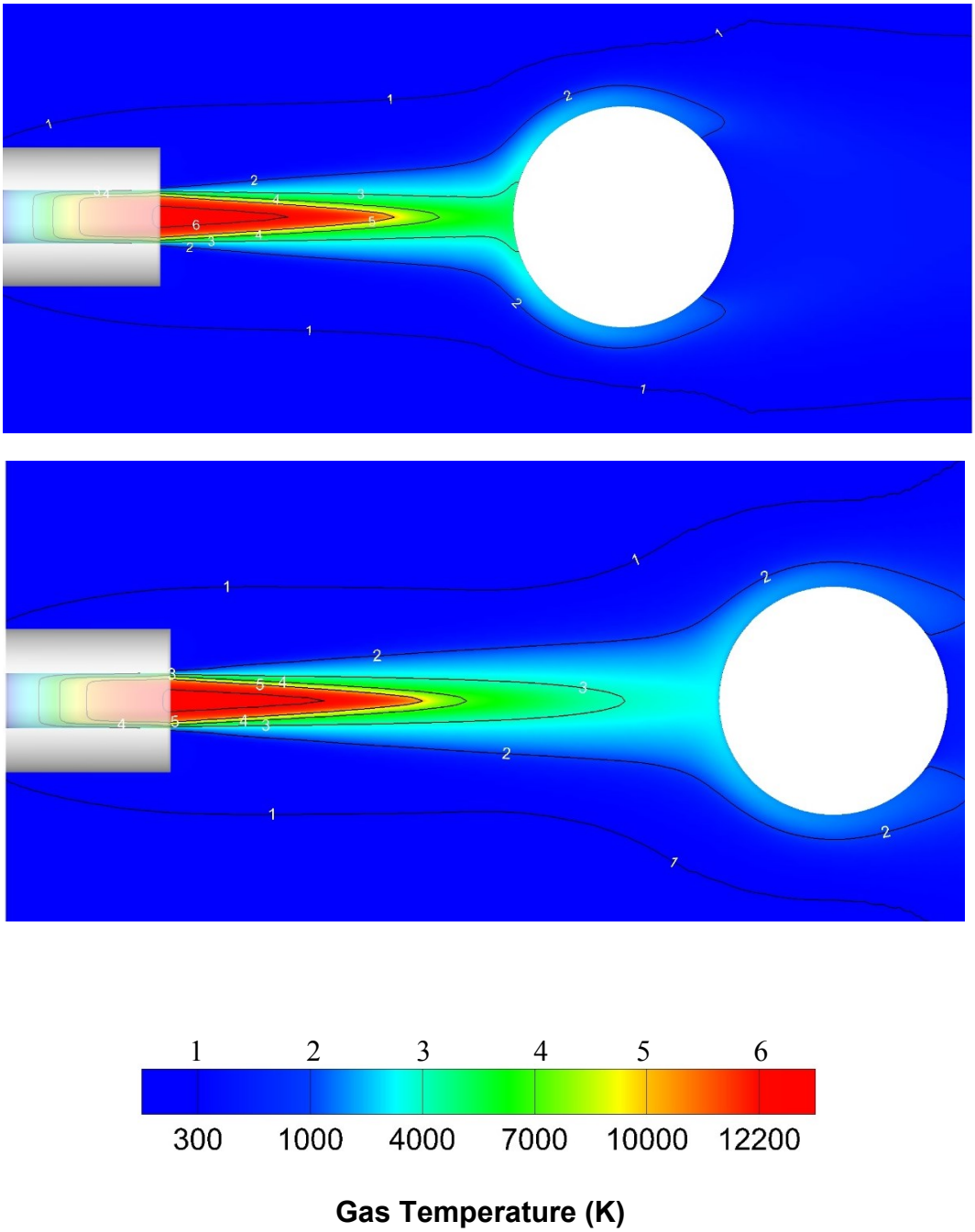

Figure 3.10 Plasma temperature contours for the curved substrates case at standoff distances of D = 4 cm and D = 6 cm

3.2. Particle phase

In order to verify the multicomponent heat transfer, a case is created in which a 40 micron droplet containing zirconia (%10 wt.) and ethanol is used. Droplet is located at the center of the nozzle exit plane inside a steady undisturbed plasma flow. For simplicity in this case, droplet break up is not considered. Figure 3.11 shows the evolution of the droplet temperature as a function of time while the droplet is traveling inside the plasma. Figure 3.11 (a) indicates that, after the ethanol is evaporated, the particle temperature increases up to nearly 4000 K and then starts to cool down as it continues its path along the centerline. In order to capture the melting of the zirconia particle, flow time step is decreased in another case as demonstrated by Figure 3.11 (b). In this Figure, the first plateau represents the time that is needed for the evaporation of the ethanol and the second plateau corresponds to the melting of the zirconia particles which occurs faster compared to evaporation of the ethanol. The second part of this project is dedicated to the modeling of the suspension injection and its interaction with the plasma jet. To do so, in this study instead of injecting suspension in form of a continuous jet, a train of fragmented droplets with a uniform size of 150 μm (same as the injector) diameter and velocity of 30 m/s are injected radially with a backward angle of $\theta = 14^{o}$ with respect to the normal plane to the plasma plume (as shown in Figure 3.12). Droplets are injected with a sequence of 3.2 μs to provide the same suspension mass flow rate used in the experimental setup (0.5 gr/s). Figures 3.13 and 3.14 show the particles trajectories and their temperature distributions in space after they interact with the plasma jet. Suspension droplets are injected in three different cases: 1) in a free jet (Figure 3.13), 2) with the inclusion of a flat substrate (Figure 3.14-a) and 3) with the inclusion of a curved one (Figure 3.14-b).

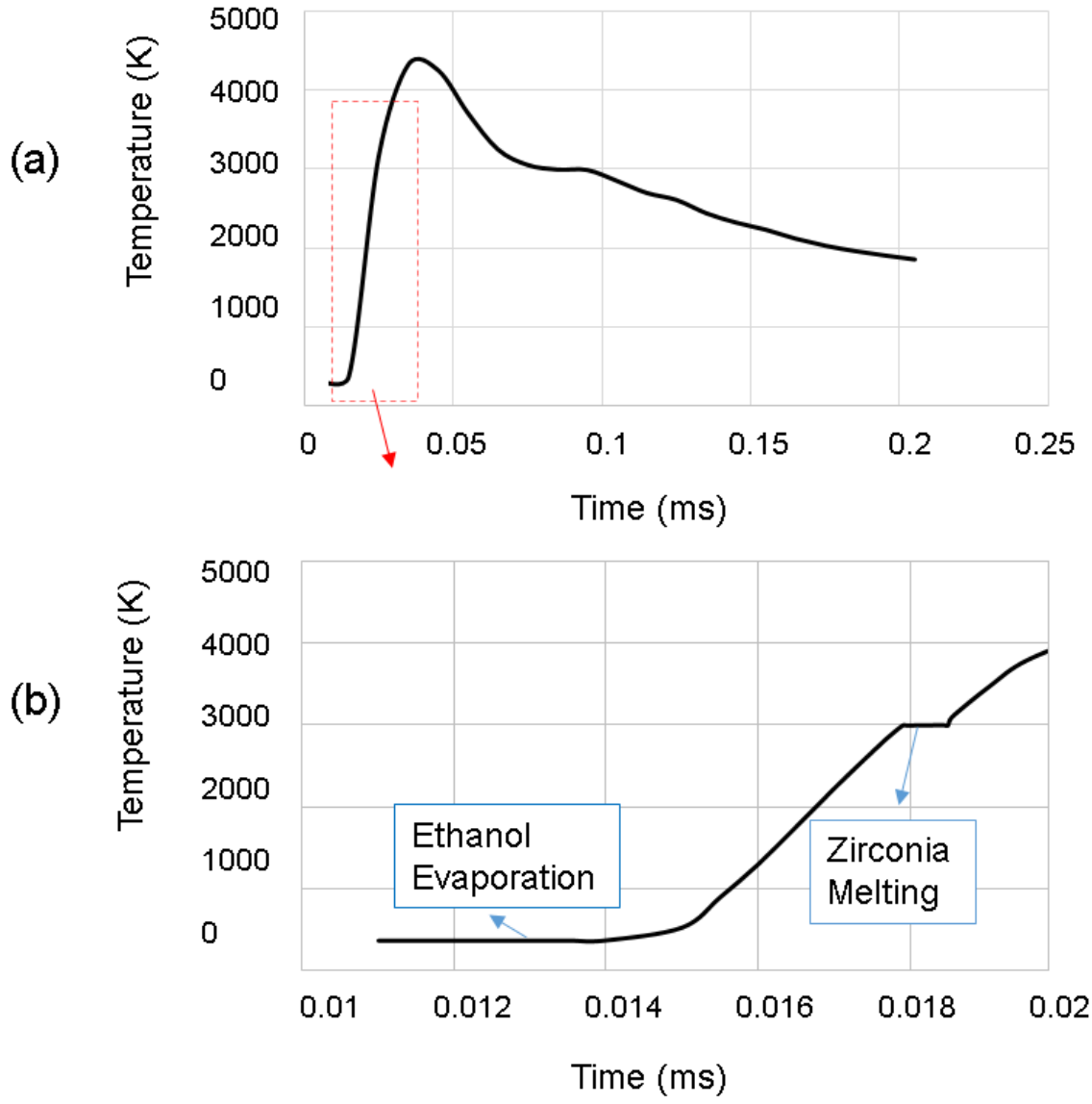

Figure 3.11 Evolution of the temperature of a 40 μm particle as a function of time

These distributions are accompanied by the plasma gas temperature contour to examine the interaction between plasma gas and injected droplets at the same time. The particle size in above mentioned figures represents the original particles size magnified 400 times. Figure 3.13 shows the suspension injection into a free jet and inflight particles trajectories that are

traveling along the plasma gas without feeling any disturbance caused by inclusion of substrate.

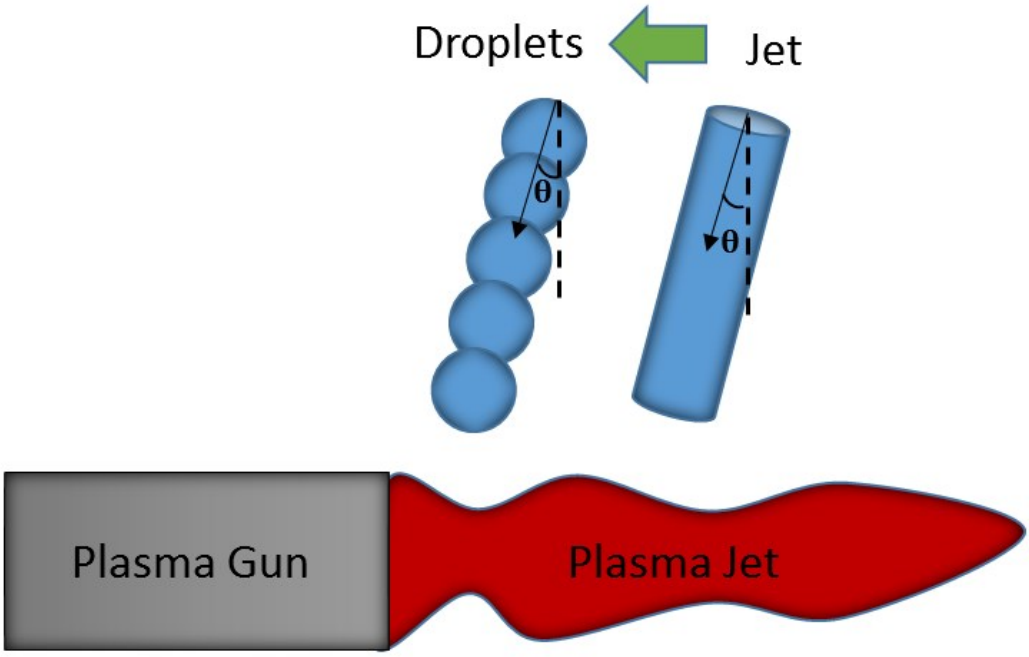

Figure 3.12 Schematic suspension injection into the plasma plume

It can be observed that those fine particles (~0.5-2 μm) that are located near the torch centerline gained higher temperature comparing to the rest of the particles that are traveling in the fringes of the plasma plume. Particles that are traveling in the fringes of the plasma are those that do not penetrate deeply in the plasma plume and consequently stay in larger sizes compared to the rest.

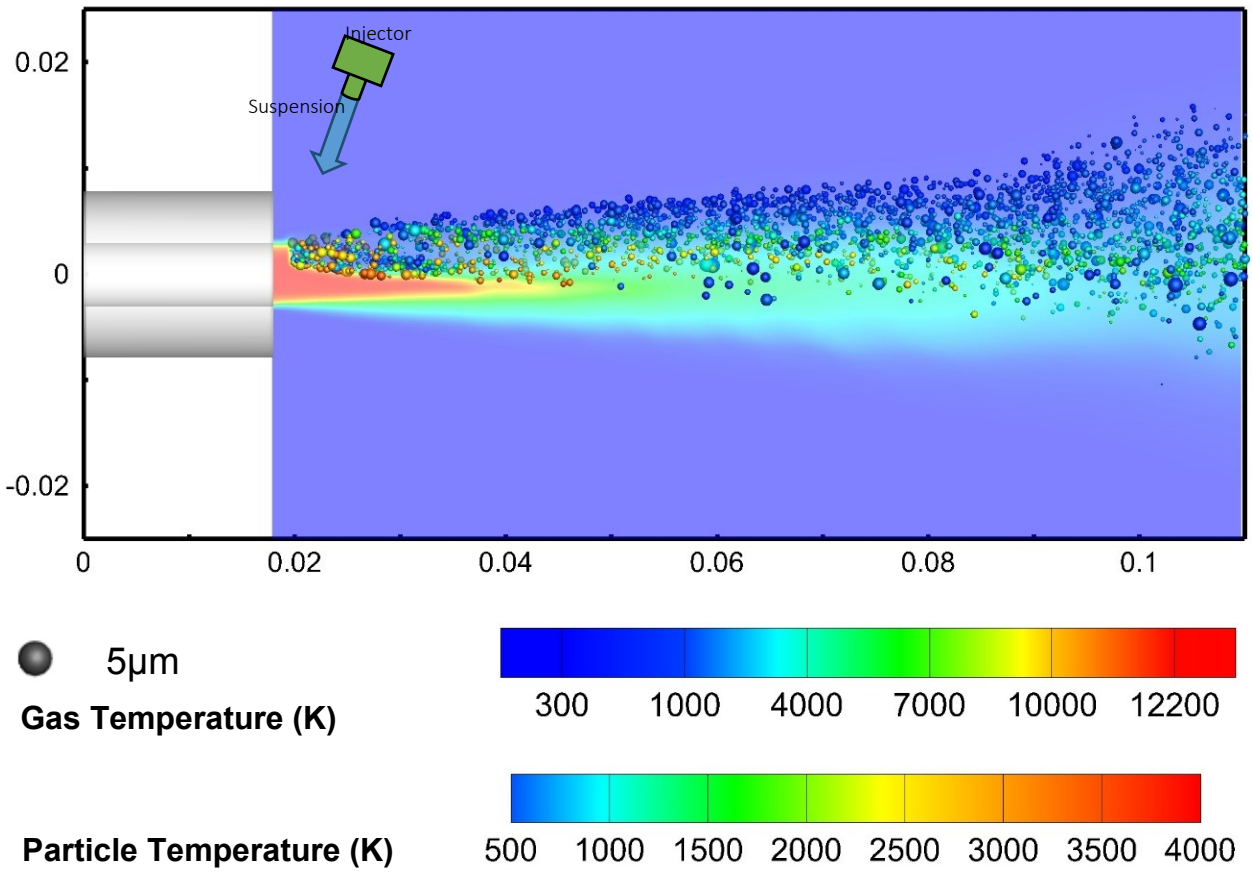

Figure 3.13 Plasma temperature contours with particle temperature injected in free jet (dimensions in the above figure are in meters).

Moreover, the effect of insertion of a flat and a curved substrate on inflight particles are shown in Figure 3.10 (b), (c) respectively. It should be noted that the trajectories of smaller sized particles (below 2 µm) are more influenced by the change of the flow pattern caused by the insertion of substrate as it can also be seen in Figure 3.14 (a) and (b). These small particles also gain higher temperature compared to the larger ones.

It should also be noted that most particles pass over the upper part of the flat and the curved substrate indicating that suspension injection conditions are not optimal. Due to the high melting point of zirconia particles (around 3000 K) many of them do not become fully

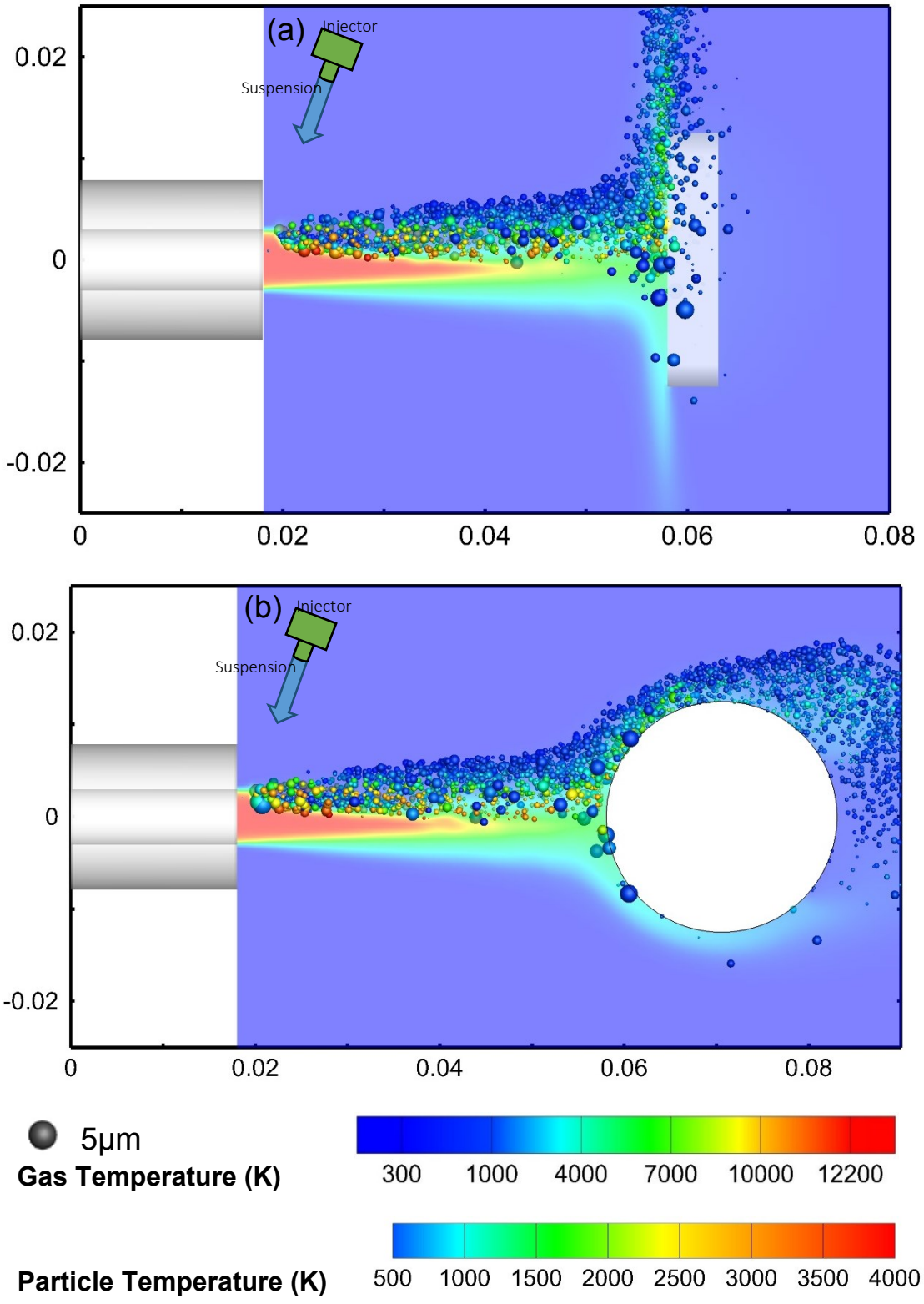

Figure 3.14 Plasma temperature contours with particle temperature including (a) flat and (b) curved substrate located at D = 4 cm(dimensions in the above figure are in meters).

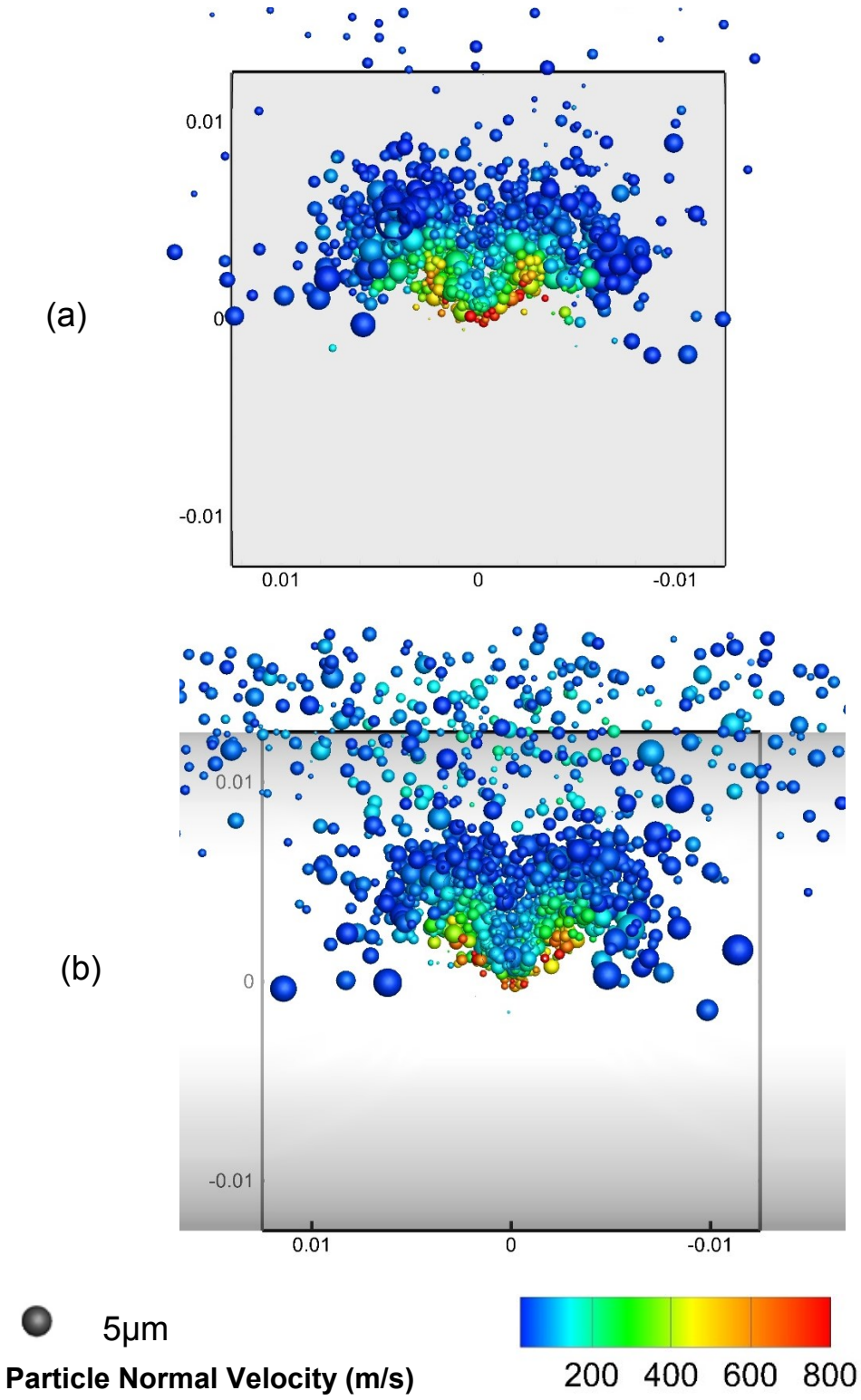

Figure 3.15 Particle normal velocity upon impact on (a) flat and (b) curved substrate (dimensions in the above figure are in meters).

molten before striking on the substrate (see in Figure 3.14 (a) and (b)) which can result in rather small deposition efficiency. Figure 3.15 shows particles' normal velocity distribution 10 mm away from the nozzle exit as they are traveling along the centerline toward the substrates as seen from the nozzle exit position. Figure 3.15 demonstrates three different zones for particles velocity. A high velocity zone (500-800 m/s) for particles that are close to the centerline, a low velocity zone (~100 m/s) containing particles that are surrounding the plume rather than being inside it and between them there is an intermediate velocity zone in which particles are traveling inside the plasma plume with velocities of 200-400 m/.It would be expected that the quality of the resultant coating would decrease as the number of the particles in the low velocity zone increases.

3.2.1. Effect of changing the standoff distance

In this section, effect of changing the flat substrate standoff distance (D = 4 cm and D = 6 cm) on particles' characteristics in the vicinity of the substrate is discussed.

Figures 3.16 and 3.17 show the particles' landing location, temperature, normal velocity and a size scale in a $25\times25\times0.2$ mm^3 rectangular box located in front of the flat substrate at 4 and 6 cm standoff distances. By inspecting the results at D = 4 cm, it is evident that high temperature (molten) and high velocity particles are traveling close to the centerline. These particles cool down and decelerate by increasing the standoff distance (D = 6 cm). Particles with relatively low temperature and velocity correspond to the suspension drops that do not penetrate efficiently into the plasma plume and are travelling in low-temperature zones that surround the plasma plume.

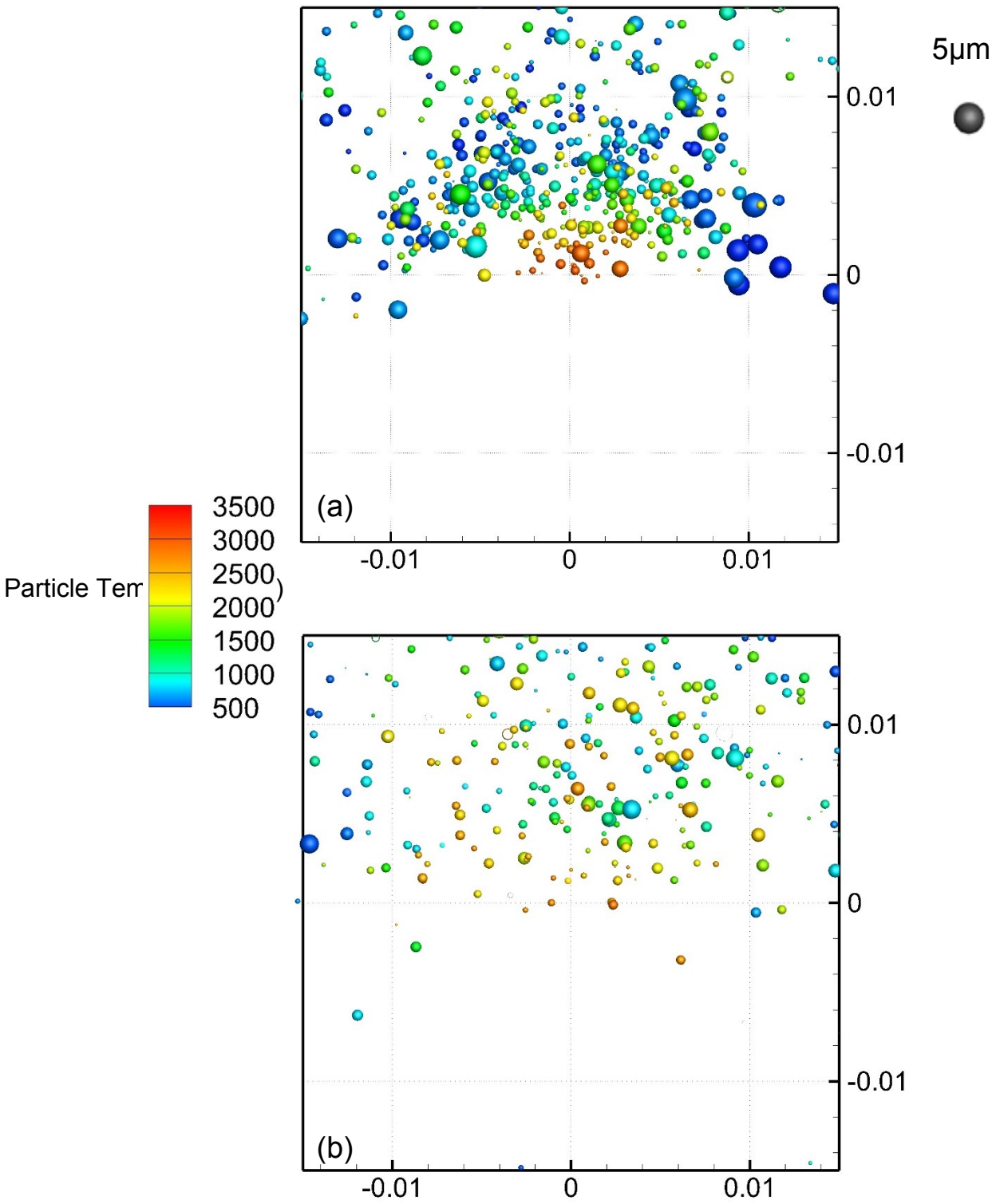

Figure 3.16 Landing location, particle temperature and size distributions on the flat substrate for standoff distances of (a) D = 4 and (b) D = 6 cm (dimensions in the above figure are in meters)

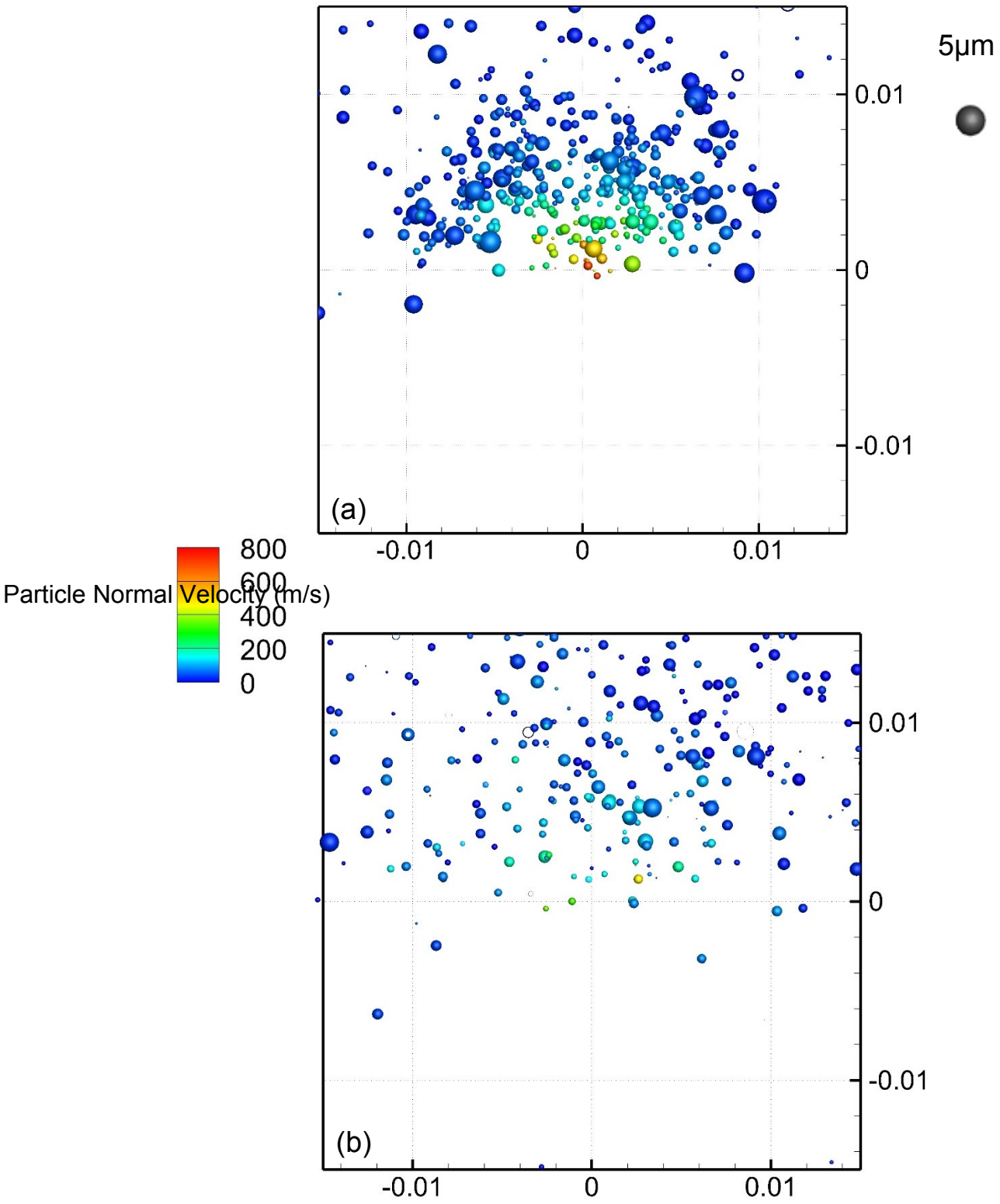

Figure 3.17 Landing location, particle normal velocity and size distributions on the flat substrate for standoff distances of (a) D = 4 and (b) D = 6 cm (dimensions in the above figure are in meters)

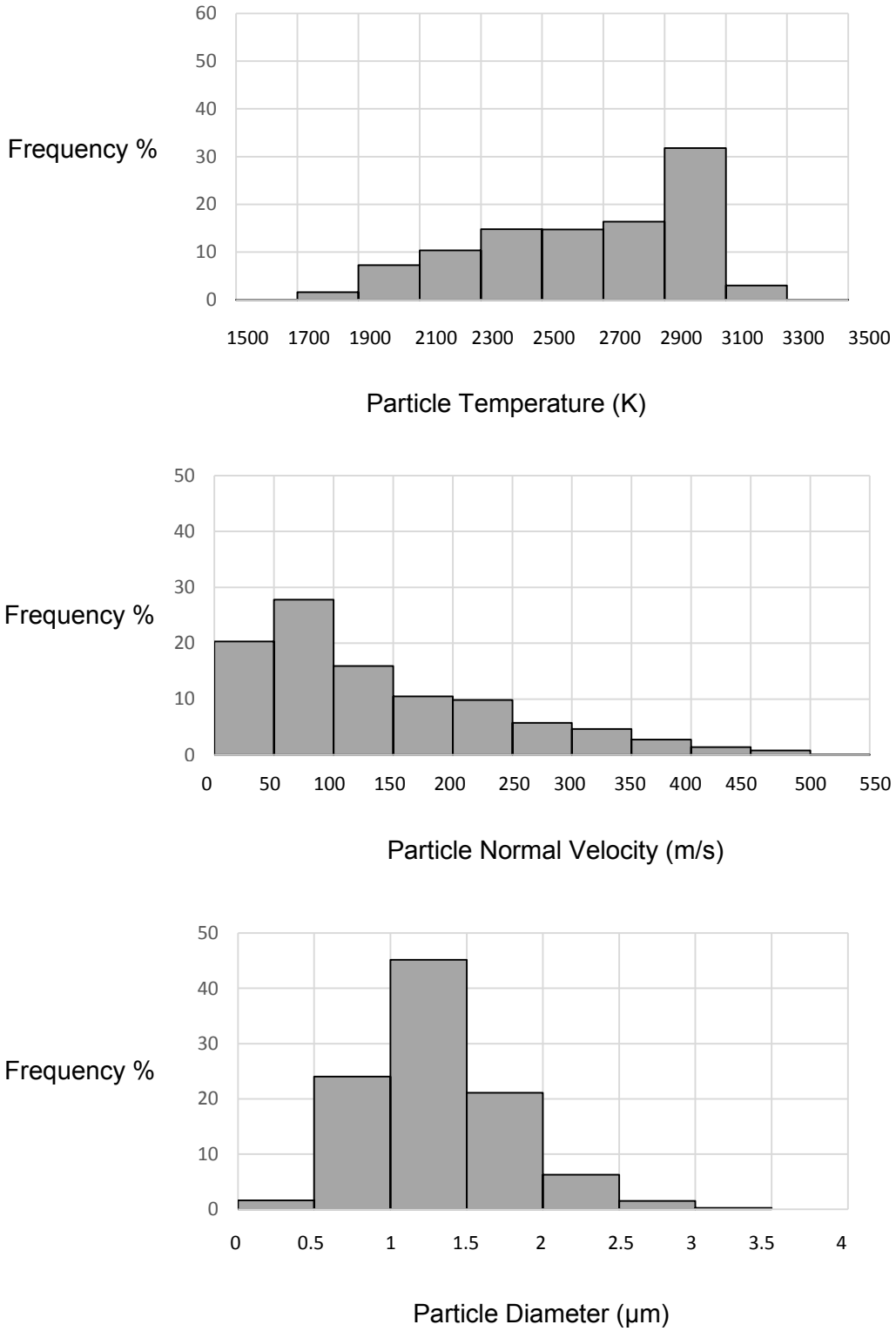

Figure 3.18 Quantitative analysis on the temperature, velocity and diameter of sprayed particles landing on the surface of a flat substrate at standoff distances of D = 4 cm

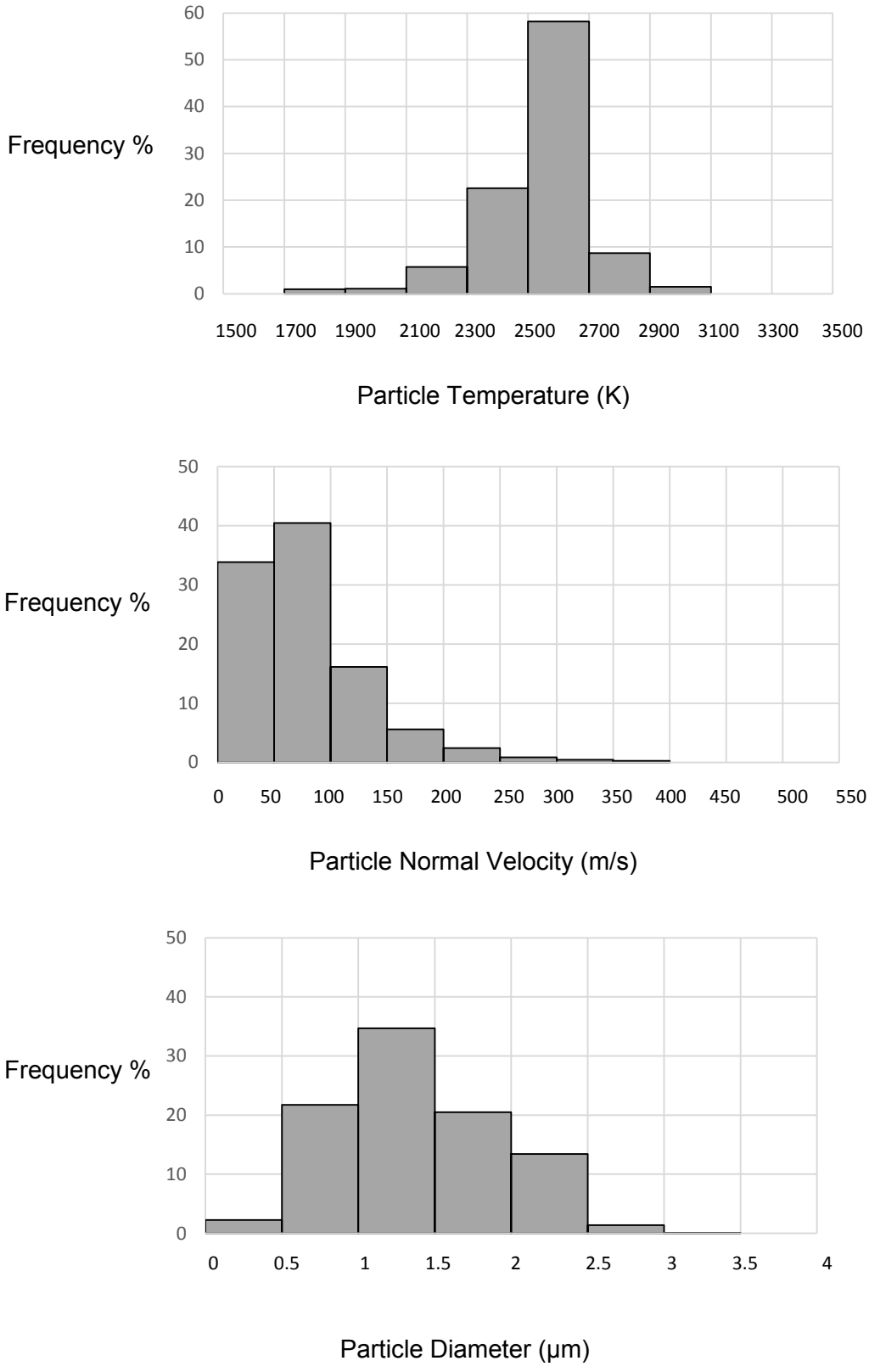

Figure 3.19 Quantitative analysis on the temperature, velocity and diameter of sprayed particles landing on the surface of a flat substrate at standoff distances of D = 6 cm

Consequently, these particles may generate defects in the produced coatings by SPS. The deviation of particles from the center is much more evident for the case at 6 cm standoff distance. Based on the observations above, it can also be expected that denser coatings will be produced at a shorter standoff distance (4 cm) as compared to 6 cm.

In order to perform a quantitative analysis on the particle data landing on the surface of the flat substrate, a surface (25mm×25mm) located on the front surface of the flat substrate is chosen. Data corresponding to the particles that reach this surface at two standoff distances of the 4 and 6 cm were recorded and are illustrated in Figure 3.18 and Figure 3.19. Figure 3.18 shows that more than 30% of the incident particles on the flat substrate are in a molten state. The high melting point of zirconia and, evaporation of zirconia particles are examples among numerous factors that have influence on the quantity of molten particles. As it can be seen from Figure 3.19, particles' temperature dropped below the melting point by increasing the standoff distance to D = 6 cm. Deviation of particles from the centerline along with rapid decrease in plasma gas temperature could explain the presence of the high number of non-molten particles in the case of D = 6 cm. Figure 3.18 and Figure 3.19 also illustrate the particle normal velocity distribution at both spray distances. As shown in these figures, the particles will impact the flat substrate with higher normal velocity at D = 4 cm compared to D = 6 cm. This is expected since the plasma axial velocity decreases along the centerline as standoff distance increases. Consequently, particles would decelerate by increasing the standoff distance and hit the surface with lower normal velocity. Moreover, Figure 3.18 shows that the most probable particle diameter range is 1 -1.5 μm for incident particles at D = 4cm. However as it can be seen in Figure 3.19, at D = 6 cm the diameter distribution shifts slightly to higher values. As seen above, particles at longer standoff

distances acquire lower normal velocity, therefore smaller particles tend to deflect more which results in a larger size distribution on the substrate at D= 6 cm.

Consequently, from the discussion above it can be concluded that particles at 4 cm standoff distance contribute more in creating a uniform coating by having higher temperature and velocity compared to the case at a standoff distance of D=6 cm. It was also observed in the relevant experimental tests that a better coating quality is obtained at around 4 cm standoff distances [37].

3.2.1. Effect of changing the suspension mass flow rate

This section is dedicated to the investigation of the effect of changing the suspension mass flow rate on in-flight particles' trajectories and properties in the case with an obstruction of a flat substrate located at 4 cm standoff. Figures 3.20 and 3.21 show the effect of increasing the suspension mass flow rate by 25% and 50%, respectively for cases (b) and (c) as shown in Table 3.1. By inspecting Figures 3.20 and 3.21, it is evident that in cases (b) and (c) increasing the mass flow rate has increased the penetration depth of the injected suspension droplets into the plasma due to the increase in their momentum. Furthermore, comparing to case (a), case (b) shows a higher penetration depth and as a

Case	Mass flow rate (g/s)
a	0.5
b	0.625
c	0.75

Table 3.1 Suspension mass flow rate (a) 0.5, (b) 0.625 and (c) 0.75 g/s

consequence of a more severe fragmentation of the droplets, smaller particle size distributions are obtained in Figures 3.20 (b). Another important observation from Figures 3.20 and 3.21 is that the quantity of cold particles which corresponds to those that did not penetrate inside the plasma gas has significantly decreased. In addition, since the particles are closer to the centerline in case (b), they will acquire higher normal velocities compared to case (a) which results in a lower residence time in the plasma jet. Moreover, increasing the suspension mass flow rate has shortened the length of the plasma plume or, in other words, the plasma jet has cooled down compared to case (a) as it can be seen in Figures 3.20 (b) and 3.21 (c). This could weaken the positive effect of the higher penetration depth on the particles' temperature and velocity. Case (c) shows the example of an excessive increase in suspension mass flow rate. From Figure 3.21 (c), it is apparent that too much suspension penetration into the plume has significantly cooled down and disturbed the entire plasma high temperature core.

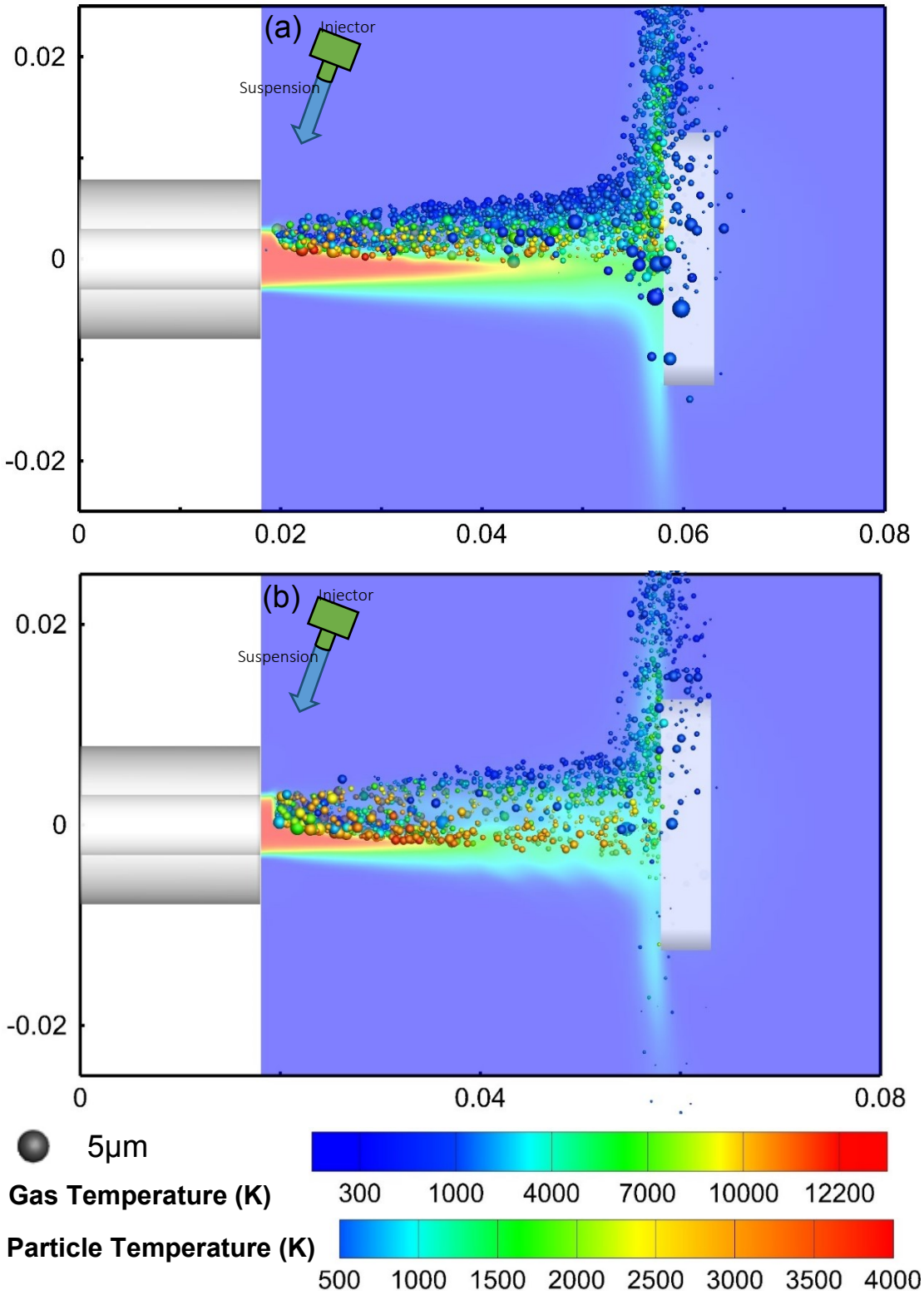

Figure 3.20 Plasma temperature contours with temperature of the injected particles in case of flat substrate with mass flow of (a) 0.5 and (b) 0.625 g/s at D = 4 cm(dimensions in the above figure are in meters)

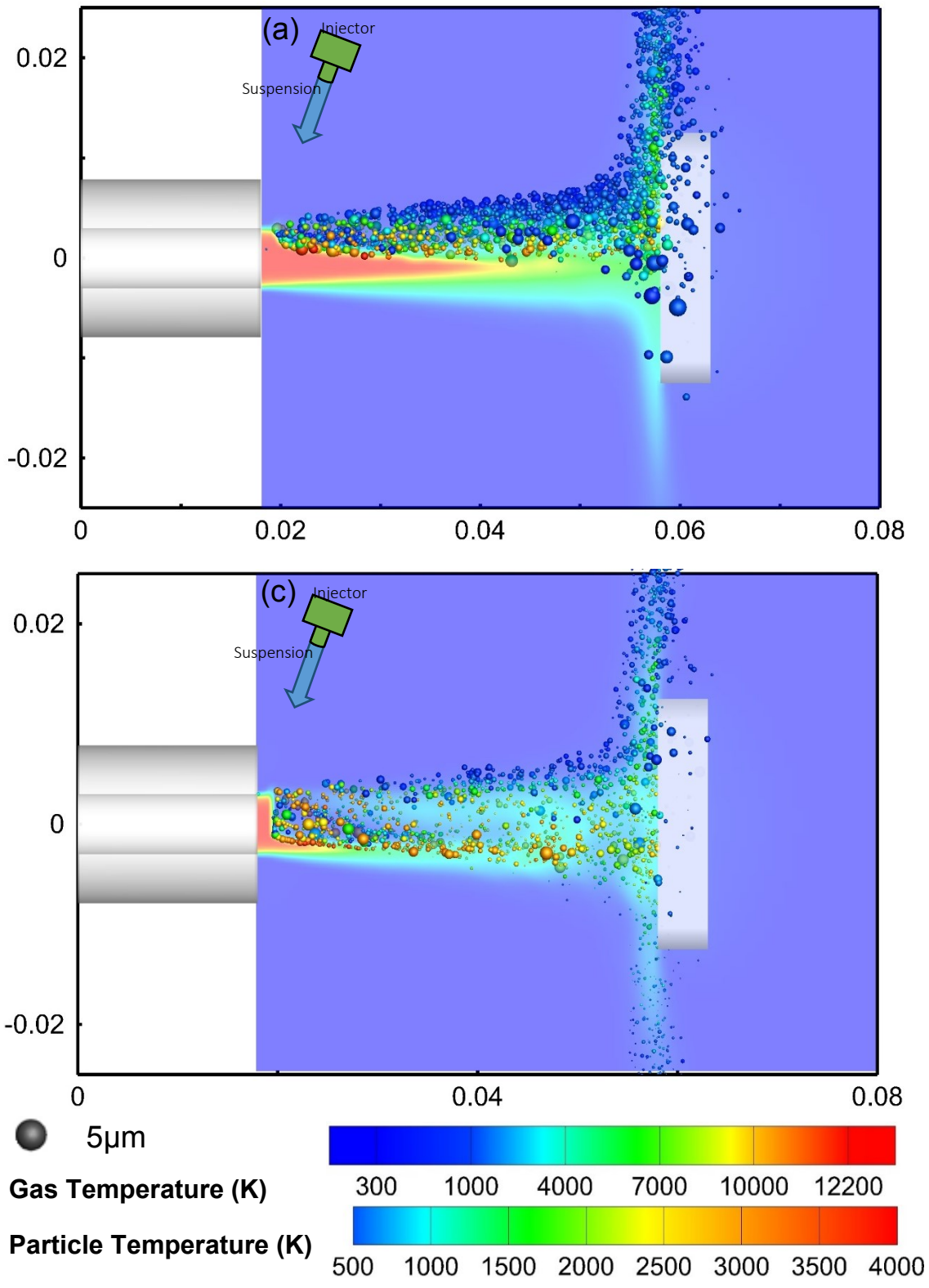

Figure 3.21 Plasma temperature contours with temperature of the injected particles in case of flat substrate with mass flow of (a) 0.5 and (c) 0.75 g/s located at D = 4 cm(dimensions in the above figure are in meters)

Figures 3.22, 3.23 and 3.24 show a comparison between the temperature, velocity and diameter of the landed particles on the substrate in these three cases. By comparing these figures, it is evident that overall, higher temperature and velocity distributions are obtained in case (b) compared to cases (a) and (c) which makes case (b) an optimal condition for suspension injection. This is due to the better penetration of the injected particles into the plasma plume and the fact that they are traveling closer to the high temperature and velocity plasma core. Moreover, in case (a), penetration of the suspension is not adequate so particles gained lower temperature and velocity compared to case (b). However, in case (c) since the length of the plasma has considerably shortened, the number of particles that are traveling inside the plasma plume is reduced. This would decrease the interaction time of the droplets with the jet and consequently decrease their temperature and velocity which would lead to a poor coating deposition efficiency on the substrate. Increasing the suspension mass flow rate as stated before resulted in a smaller particle size distribution as it can also be seen from Figure 3.24. As noted before, the radius of the newly born droplets is related to the growing instabilities on the droplet surface. The presence of higher instabilities on the droplet surface in the cases (b) and (c) due to more severe interaction of the suspension with the plasma has led to smaller child droplets and consequently smaller particle size distribution compared to case (a).

From the above discussion, it can be concluded that there should be an optimum value of the mass flow rate above which suspension would cool down the plasma core leading to low temperature and velocity distribution and consequently poor coating quality.

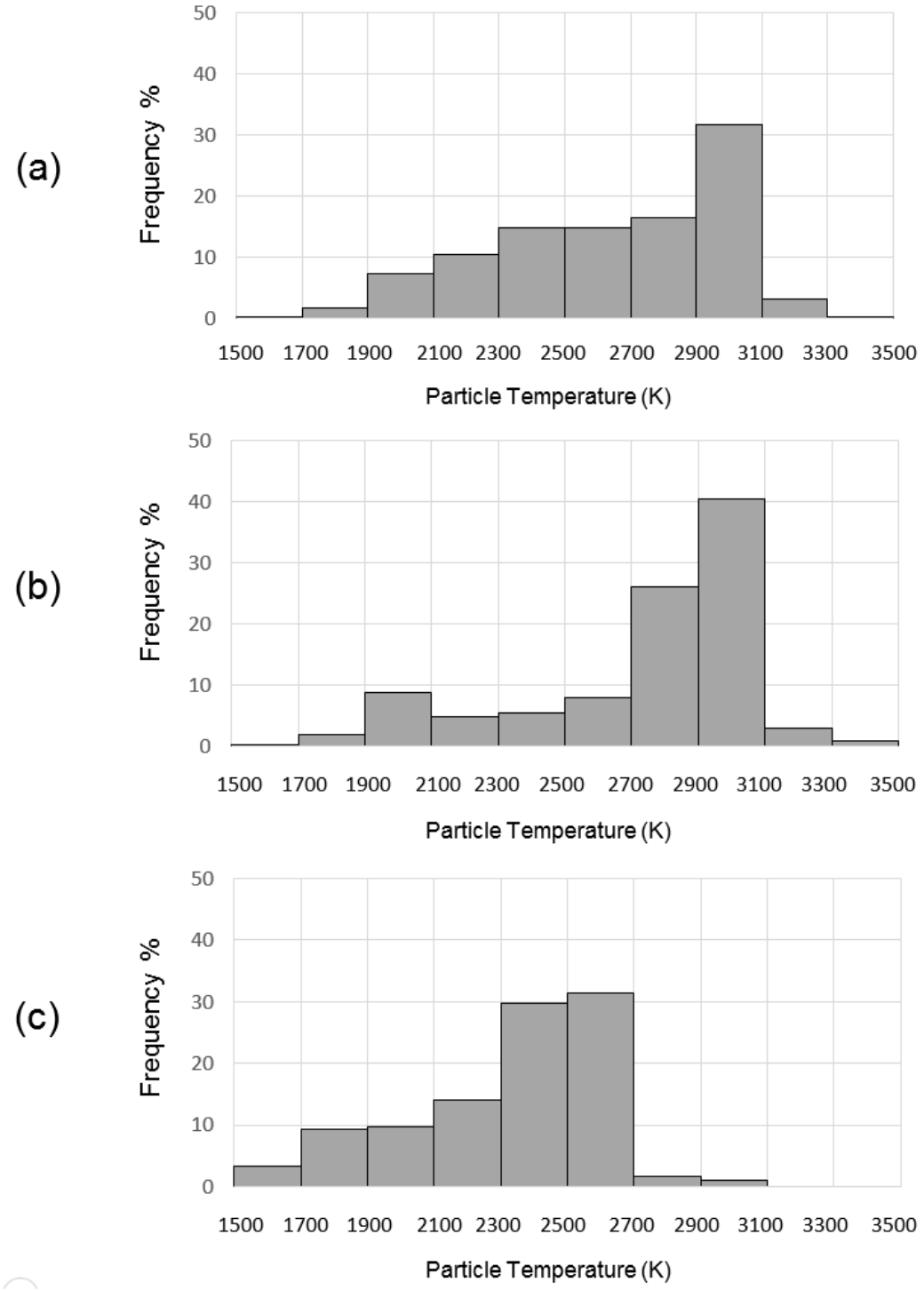

Figure 3.22 Temperature of landing particles injected in the case of flat substrate located at D = 4 cm with mass flow rates of (a) 0.5 , (b) 0.625 and (c) 0.75 g/s

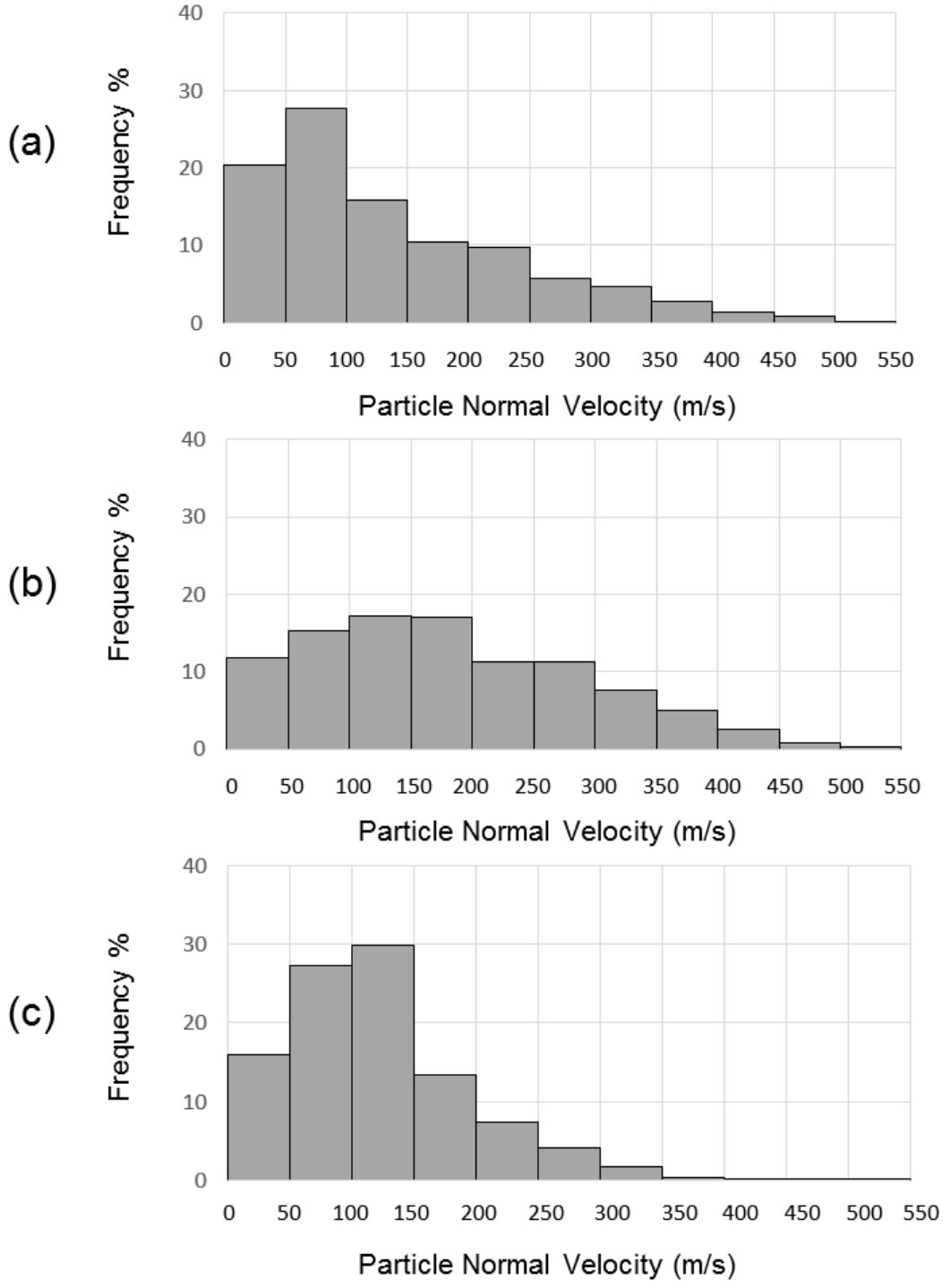

Figure 3.23 Velocity of landing particles injected in the case of flat substrate located at D = 4 cm with mass flow rates of (a) 0.5, (b) 0.625 and (c) 0.75 g/s

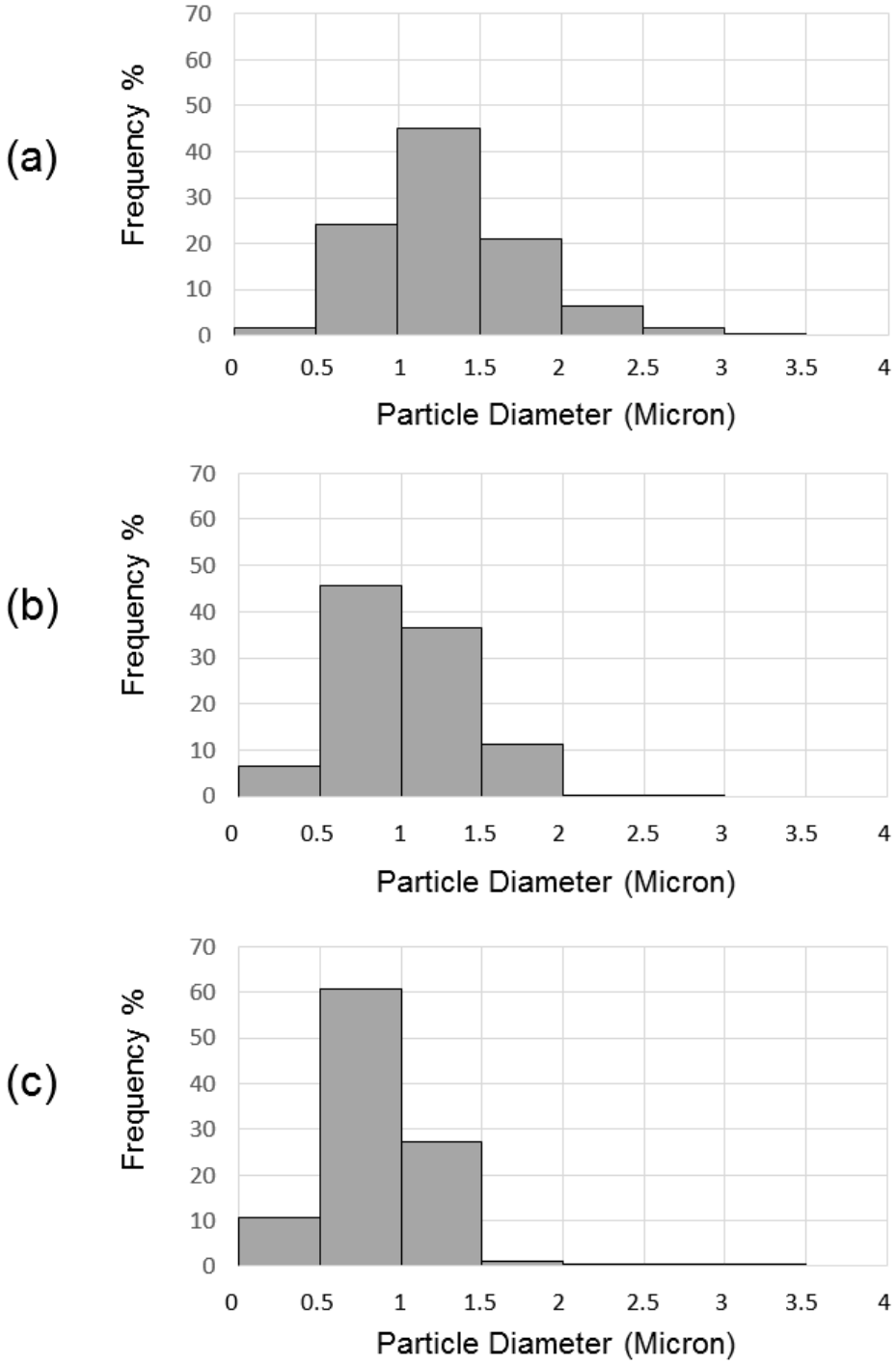

Figure 3.24 Diameter of landing particles injected in the case of flat substrate located at D = 4 cm with mass flow rates of (a) 0.5, (b) 0.625 and (c) 0.75 g/s

3.2.2. Effect of substrate curvature

In the next step for the curved substrate located at the standoff distance of 4 cm, a surface with length L that covers the front surface of the cylinder as shown in the Figure 3.25 is chosen to record the data associated with particles landing on the substrate. Similar to the case of the flat substrate, quantitative analyses on landed particles on the curved substrate is performed and results are compared with data for the flat substrate located at the same standoff distance. By inspecting the number of the incident particles in these two cases (flat and curved substrates) during a fixed time interval ($\Delta t = 1ms$) , it is interestingly observed that particles hit the flat substrate nearly 2.2 times more frequently compared to the curved one. Based on this observation a parameter called "Catch Rate" is defined by the following equation:

$$Catch\ Rate\,(\%) = \frac{mass\ of\ landed\ particles\ in\ \Delta t}{mass\ of\ injected\ particles\ in\ \Delta t} \times 100 \qquad (3\text{-}1)$$

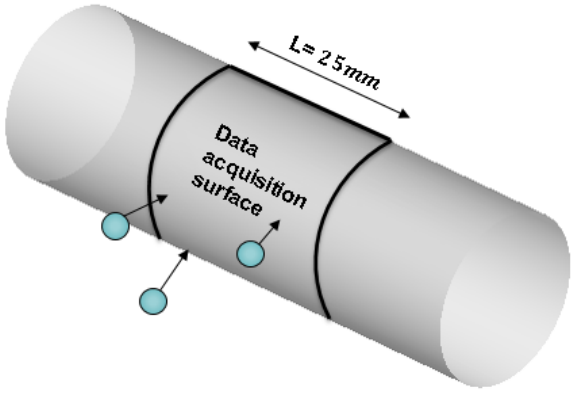

Figure 3.25 Acquisition data region on the curved substrate

The observed catch rate on the flat substrate is 23% while it decreases to 11% on the curved substrate. This significant catch rate decrease on the curved substrate would result in a much lower amount of coating deposition on the curved substrate.

In addition, it is expected that the normal component of the particle impact velocity has a major influence on the deposition of the particles landing on a flat substrate. Using the same analogy, the distribution of the particle normal velocity components, V_n, is investigated in this study for the curved substrate. This is further explained with the schematic view shown in Figure 3.26.

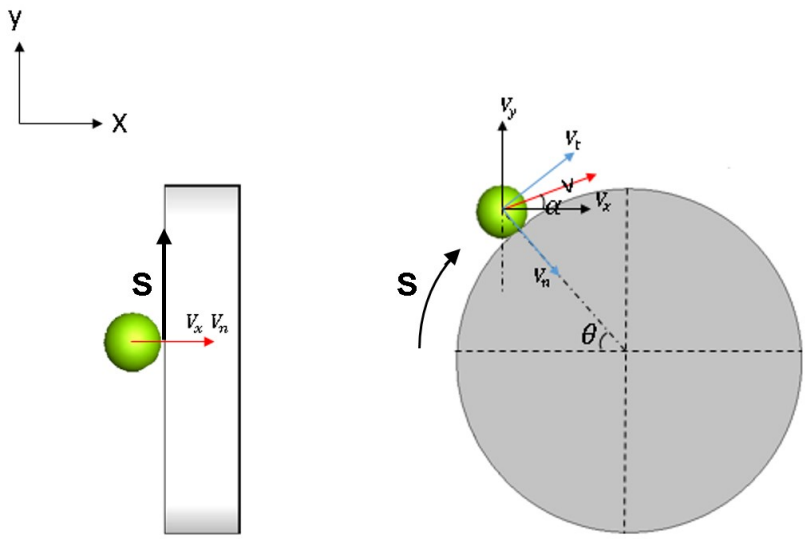

Figure 3.26 Particle normal velocity on flat and curved substrates

The results for particles' normal velocity distribution for the two different substrates (flat and curved) at D = 4 cm as a cumulative percentage is illustrated in Figure 3.27. This figure indicates that particles tend to hit the flat substrate with a slightly higher normal velocity compared to the curved substrate. Figure 3.28 presents a comparison between particle

temperatures landing on the two different substrates located at 4 cm standoff distance. The increase in the quantity of molten particles landed on the curved substrate could be due to the milder turning of the flow around the cylinder. Furthermore, the distribution of the particle landing location on flat and curved substrates at D = 4 cm along the distance (S as shown in Figure 3.26) were calculated. Then these results are compared to the results of the free jet case in which particles are going through an imaginary plane located at the same distance and dimensions as the flat substrate (25×25 mm^2). These results are shown in Figure 3.29 as a function of cumulative percentage which is calculated based on the number of the particles. It also should be noted that in Figure 3.29, the number of landing particles on the two substrates is normalized based on the number of particles passing through the imaginary surface in the free jet case. As shown in Figure 3.29, in the absence of substrates (i.e. free jet case) more than 40% of in-flight particles pass the imaginary plane at S between 0-2 mm.

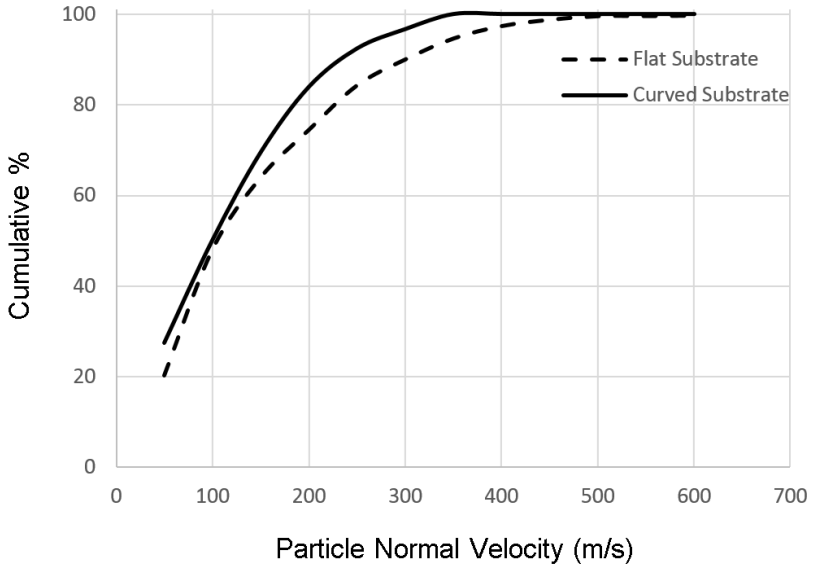

Figure 3.27 Cumulative particle normal velocity on flat and curved substrates at D = 4 cm

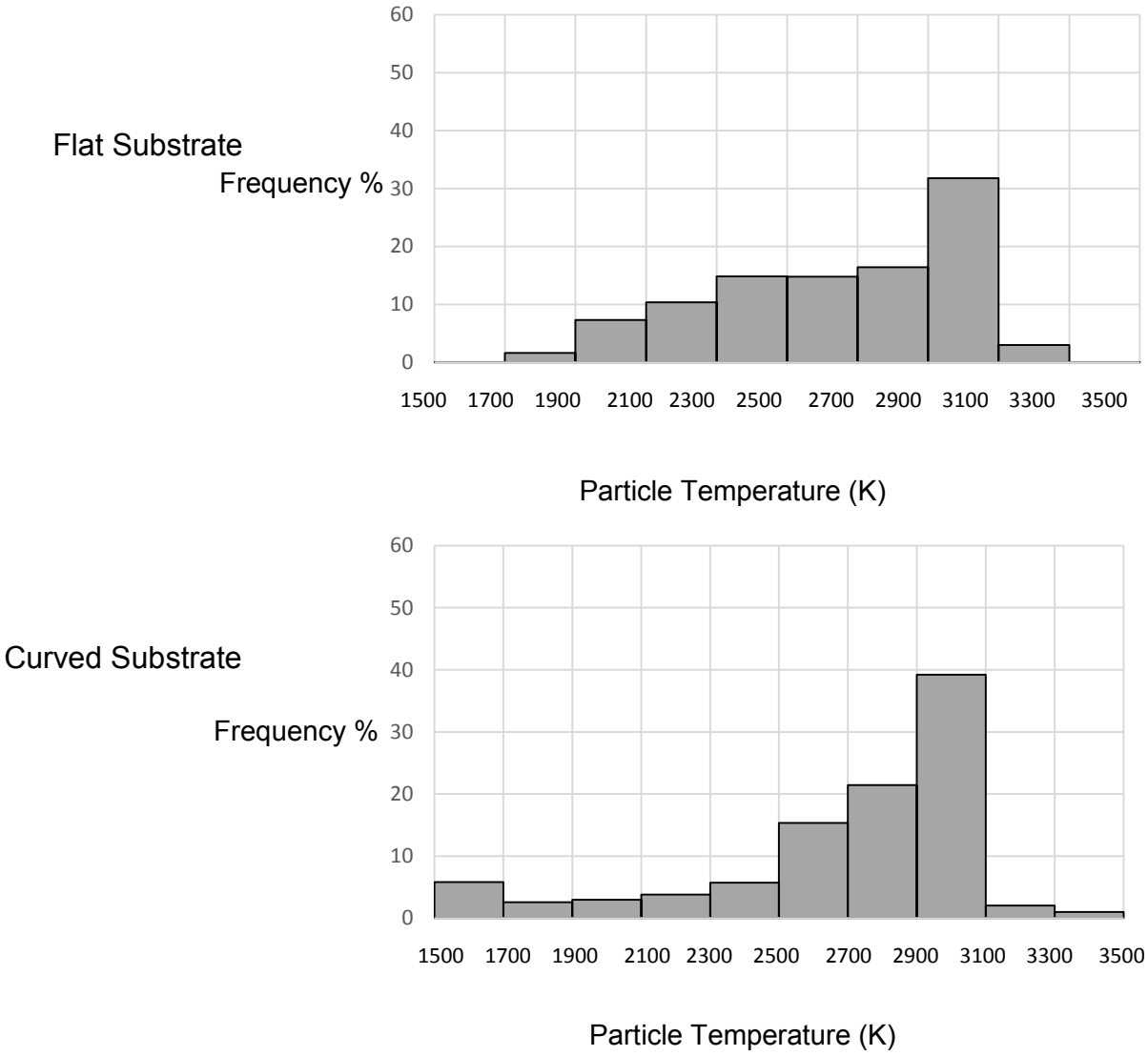

Figure 3.28 Temperature of landing particles injected in the case of flat and curved substrate located at D = 4 cm

According to Figure 3.29, adding a flat substrate scatters these in-flight particles from the centerline, shifts the pick of the graph to S values of 2-4 mm and induces a wider distribution in S direction of the particle landing location.

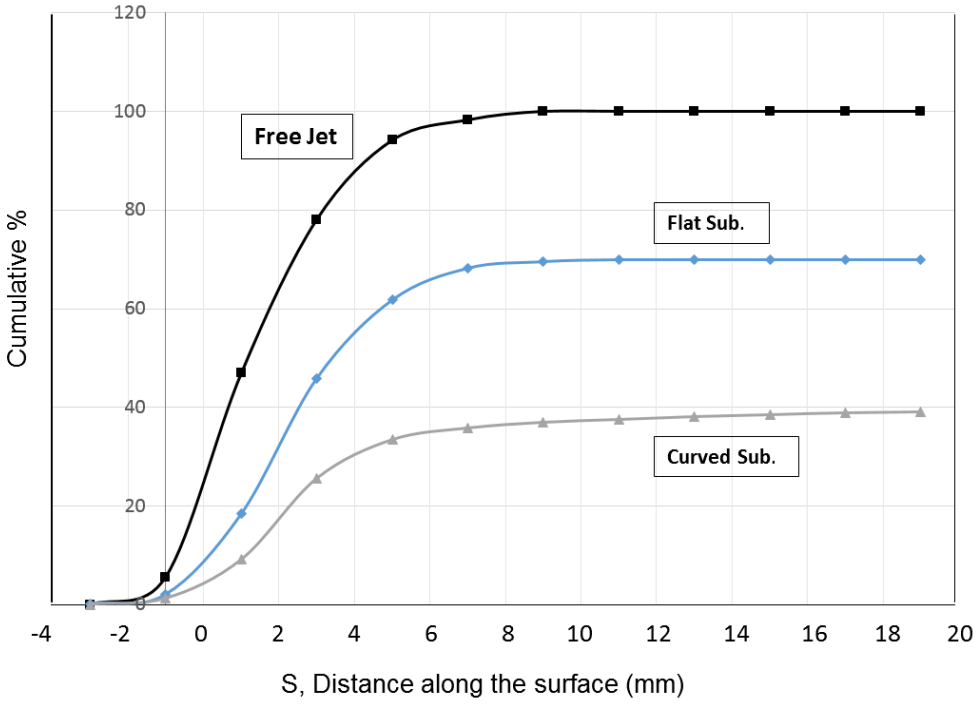

Figure 3.29 Distribution of the particle landing location in case of free jet, curved substrate and flat substrate at D= 4 cm as a function of distance along the surface, S

In the case of the curved substrate most of the in-flight particles hit the curved substrate at location of 2-4 mm $(10^{o} < \theta < 20^{o})$ and as we move along the surface (in the S direction) the number of landed particles decreases rapidly compared to the flat substrate and the free jet. Comparing the number of the landed particles on the curved substrate with the other cases in Figure 3.29, it is evident that a lower deposition rate is going to be obtained on the curved substrate compared to the flat one. The difference between Figure 3.29 and the calculated catch rates arises from the fact that the definition of the catch rate is based on the mass of the particles while in Figure 3.29 values are based on the quantity of them. It is important to note that although the catch rate of the cylinder is half of that of the flat substrate, the formation of a weaker stagnation pressure on the curved substrate will result in higher impact particle velocity specifically near the centerline.

4. Conclusion and future work

In this chapter

In this chapter, the conclusion of this study will be presented. In addition, future work will be discussed.

A 3D numerical modelling has been carried out to investigate the effect of substrate and its' shape on in-flight particle properties and trajectories. In the first step, a constant energy source is used to model the plasma flow and the results are compared with relevant experimental and numerical studies.

This study is based on a two-way coupled Eulerian-Lagrangian approach in which the solution to the gas phase obtained earlier is used for the discrete phase part. Among various available turbulence models the Reynolds Stress turbulent Model (RSM) is utilized instead of Boussinesq hypothesis since it solves all the Reynolds shear stresses. In order to model the dispersed phase, discrete phase method is used in which a large number of particles are tracked while they can exchange mass, momentum and energy with the plasma gas. Transport of suspension into the plasma plume involves complex phenomena such as droplet penetration and fragmentation. For modeling the droplet fragmentation due to the existence of the catastrophic break up mode, Kelvin-Helmholtz and Rayleigh-Taylor (KHRT) instabilities are utilized to model secondary atomization.

Since one of the aims of this work is to investigate the effect of substrate on particles' characteristics, different cases were studied to take into account the inclusion of substrate. In all these cases, temperature, velocity and size distribution of the landing particles were studied. Results of these investigations revealed that particles tend to have higher normal velocity and temperature and lower sizes at 4 cm standoff distance compared to 6 cm standoff distance. Consequently, a higher deposition is expected in lower standoff distance D = 4 cm compared to D = 6 cm which is in good agreement with the experimental observation [36]. In addition, the effect of increasing the mass flow rate of the suspension on in-flight particle characteristics were investigated. It is observed that increasing the

suspension feed rate led to a better fragmentation of droplets and resulted in an increase in particle temperature and velocity. However, it was shown that there is an optimum value for the feed rate. Excessive increase in the suspension mass flow rate was found to disturb the plasma high temperature potential core, result in low particle temperature and velocity and consequently lead to a poor deposition efficiency. Finally, the effect of changing the substrate's curvature on particles' deposition was investigated. It was found that, for a fixed time interval, particles hit the surface of the flat substrate 2.2 times more frequently compared to the curved substrate. Based on this finding a new parameter called "Catch Rate" was introduced.

Special attention was paid in this study to investigate particles impact velocity based on their normal component. A higher normal velocity is observed on the flat substrate compared to the curved substrate as expected. Furthermore, particles' landing location as a function of the distance along the surface were calculated and compared for three cases of free jet, flat and curved substrates. It was observed that most of the particles tend to hit the surface of the cylinder at angles between ($10^{o} < \theta < 20^{o}$) and above this range, particles will pass over the curved substrate without striking on it. It was also concluded that the formation of a weaker stagnation pressure on the curved substrate would result in a higher impact velocity in the stagnation region compared to the flat one.

The quantity and level of complexity of the phenomena involved in suspension plasma spraying (plasma flow generation, liquid-jet interaction, particles agglomeration and solidification and etc.) have made it difficult to find a global numerical model which is capable of simulating the whole SPS process at once. However, there are some future steps

which can improve and strengthen the capabilities of this model. Some of these steps are summarized as follows,

- Due to the arc movement inside the torch, plasma flow has transient nature and is unsteady. As it can be seen in this study, this model has successfully captured the particles' characteristics by assuming an average condition (power) for the plasma gas which is in reasonable agreement with the experimental measurements. However, finding a model that can best describe the arc attachment along with its movement inside the plasma gun could improve this work.
- Plasma gas can be modeled in Non Local Thermodynamic Equilibrium (NLTE) condition instead of LTE assumption.
- In this study, it was assumed that suspension is leaving the injector as equally sized uniform droplets. However, in reality, the suspension is leaving the injector as a liquid jet that is further fragmented to droplets due to the primary atomization. Therefore, modeling the primary atomization as future work could give a more accurate size distribution for the fragmented droplets.

References

1. **Davis, J.R.**, *Handbook of Thermal Spray Technology*, Materials Park, OH, ASM International, 2004.

2. **Fauchais, P., Heberlein, J.V.R and Boulos, M.I.,** *Thermal Spray Fundamentals*, Springer, 2014.

3. **Leblanc, L., and Moreau, C.,** *The Long-Term Stability of Plasma Spraying*, Journal of Thermal Spray Technology, Vol. (3) pp 380-386, 2002.

4. **Fazilleau, J., Rat, C. V., Coudert, J.F., Fauchais, P. and Pateyron, B.** *Phenomena Involved in Suspension Plasma Spraying Part 1: Suspension Injection and Behavior*, Journal of Plasma Chemistry Plasma Processing, Vol. 26(4), pp 371-391, 2006.

5. **Fauchais, P., Etchart-Salas R., Rat, V., Coudert, J.F., Caron, N. and Wittmann-Ténèze, K.,** *Parameters controlling liquid plasma spraying: Solutions, sols, or suspensions*, Journal of Thermal Spray Technology, Vol. 17(1), pp 31-59, 2008.

6. **Berghaus, J. O., Bouaricha, S., Legoux, J. G. and Moreau, C.,** *Injection conditions and in-flight particle states in suspension plasma spraying of alumina and zirconia nano-ceramics*, Proceedings of the International Thermal Spray Conference, Basel Switzerland, CD-ROM, pp 512-518, 2005.

7. **Tarasi, F., Medraj, M., Dolatabadi, A., Berghaus, J. O. and Moreau, C.,** *Effective parameters in axial injection suspension plasma spray process of*

alumina-zirconia ceramics, Journal of Thermal Spray Technology, Vol. 17(5-6), pp 685-691, 2008.

8. **Mauer, G., Vassen, R., and Stover, D.,** *Comparison and Applications of DPV-2000 and Accuraspray-G3 Diagnostic Systems*, Journal of Thermal Spray Technology, Vol. 16(3) pp. 414-24, 2007.
9. **Chang, C. H., Ramshaw, J. D.,** *Numerical Simulations of Argon Plasma Jets Flowing into Cold Air*, Journal of Plasma Chemistry and Plasma Process, Vol. 13(2), pp 189-209, 1993.
10. **Bolot, R., li, J. and Coddet, C.**, *Some Key Advice for the Modeling of Plasma Jets Using Fluent*, Proceedings of the International Thermal Spray Conference, pp 1367-1371, 2005.
11. **Bolot, R., li, J. and Coddet, C.,** *Modeling of Thermal Plasma Jet: A Comparison Between PHOENICS and FLUENT,* International Thermal Spray Conference, pp 764-769, 2004.
12. **Shan, Y., Coyle, T. W. and Mostaghimi, J.**, *Numerical simulation of droplet breakup and collision in the solution precursor plasma spraying*, Journal of Thermal Spray Technology, Vol. 16(5-6), pp 698-704, 2007.
13. **Seleven, B., Ramachandran, K., Pillai, B. C. and Subhakar, D.,** Numerical Modeling of Ar-N_2 Plasma Jet Impinging on a Flat Substrate, Journal of Thermal Spray Technology, Vol. 20(3), pp 534-548, 2011.
14. **Jabbari, F., Jadidi, M., Wuthrich, R. and Dolatabadi, A.,** *A Numerical Study of Suspension Injection in Plasma-Spraying* Process, Journal of Thermal Spray Technology, Vol. 23(1-2), pp 3-13, 2014.

15. **Jadidi, M., Mousavi, M., Moghtadernejad, S. and Dolatabadi, A.,** *A Three-Dimensional Analysis of the Suspension Plasma Spray Impinging on a Flat Substrate*, Journal of Thermal Spray Technology, Vol. 24(1-2), pp 11-23, 2014.
16. **Remesh, K., Yu, S. C. M., Ng, H. W. and Berndt, C.C.,** *Computational study and experimental comparison of the in-flight particle behavior for an external injection plasma spray process*, Journal of Thermal Spray Technology, Vol. 12(4), pp 508-522, 2003.
17. **Meillot, E., Guenadou, D., and Bourgeois, C.,** *Three-dimension and transient DC plasma flow modeling*, Journal of Plasma Chemistry and Plasma Process, Vol. 28(1), pp 69-84, 2008.
18. **Marchand, C., Vardelle, A., Mariaux, G., Lefort, P.,** *Modelling of the plasma spray process with liquid feedstock injection*, Journal of Surface Coating Technology, Vol. 202(18), pp 4458-4464, 2008.
19. **Meillot, E., Damiani, D., Vincent, S., Caruyer, C., and Caltagirone, J. P.,** *Analysis by modeling of plasma flow interactions with liquid injection*, Journal of Surface Coating Technology, Vol. 220, pp 149-156, 2013.
20. **Kang, C. W., Ng, H. W. and Yu, S. C. M.,** *Comparative study of plasma spray flow fields and particle behavior near to flat inclined substrates*, Journal of Plasma Chemistry and Plasma Process, Vol. 26(2), pp 149-175, 2006.
21. **Ba, T., Kang C. W., Ng, H. W.,** *Numerical Study of the Plasma Flow Field and Particle In-flight Behavior with the Obstruction of a Curved Substrate*, Journal of Thermal Spray Technology, Vol. 18(5-6), pp 858-874, 2009.

22. **Colombo, V., Ghedini, E.,** *Time-dependent torch: Anode attachment and downstream region effects*, Proceedings of the 17th International Symposium on Plasma Chemistry, Toronto, Canada, 2005.

23. **Trelles, J. P., Chazelas, C., Vardelle, A., and Heberlein, J. V. R.,** *Arc plasma torch modeling*, Journal of thermal spray technology, Vol. 18(5-6), pp 728-752, 2009.

24. **Boulos, M. I., Fauchais, P. and Pfender, E.** *Thermal Plasma: Fundamentals and Application*, Vol. 1, Plenum Press, New York, 1994.

25. ANSYS Inc., ANSYS-FLUENT Theory Guide, USA, 2014.

26. **Planche, M. P.,** *Experimental study of fluctuating plasma jets*, Ph.D. Thesis, University of Limoges, France, 1995.

27. **Betoule, O.**, *Relationships between the distributions of particle velocity and temperature and coating properties*, Ph.D. Thesis, University of Limoges, France, 1994.

28. **White, F. M.,** *Fluid Mechanics*, McGraw Hill Education, New York, 2008.

29. **Tanvir, S. and Qiao, L.,** *Surface Tension of Nanofluid-Type Fuels Containing Suspended Nanomaterials*, Nanoscale Research letters, Vol. 7(1), pp1-10, 2012.

30. **Morsi, S. A. and Alexander, A. J.,** *An Investigation of Particle Trajectories in Two-Phase Flow Systems* , Journal of Fluid Mechanics, Vol. 55(2), pp 193–208, 1972.

31. **Ranz, W.E. and Marshall, W.R.,** *Evaporation from Drops: Part I*, Journal of Chemical Engineering Progress, Vol. 48(3), pp 141-146, 1952.

32. **Ranz, W.E. and Marshall, W.R.,** *Evaporation from Drops: Part I and Part II*, Journal of Chemical Engineering Progress, Vol. 48(4), pp173–180, 1952.

33. **Turns, S. R.,** *An Introduction to Combustion: Concepts and Applications*, 2^{nd} edition, McGraw Hill Education, USA, 2000.

34. **Miller, R. S., Harstad, K. and Bellan, J.,** *Evaluation of Equilibrium and Non-Equilibrium Evaporation Models for Many Droplet Gas-Liquid Flow Simulations*, International Journal of Multiphase Flow, Vol. 24(6), pp 1025-1055, 1998.

35. **Reitz, R. D.,** *Mechanisms of Atomization Processes in High-Pressure Vaporizing Sprays*, Journal of Atomization and Spray Technology, Vol. 3, pp. 309–337, 1987.

36. **Viskanta, R.,** *Heat transfer to impinging isothermal gas and flame jets,* Journal of Experimental Thermal and Fluid Science, Vol. 6(2), pp 111-134, 1993.

37. **Aghasibeig, M., Mousavi, M., Ettouill, F.B., Wuthrich, R., Dolatabadi, A. and Moreau, C.**, *Electro-Catalytically Active Porous Nickel-Based Electrode Coatings Formed by Atmospheric and by Suspension Plasma Spraying*, International Thermal Spray (ITSC) Conference and Exposition, May 13-15, 2013, (Busan, Republic of Korea), 2013.